ACS OMEGA

Open Access

This article is licensed under CC-BY-NC-ND 4.0

http://pubs.acs.org/journal/acsodf

Article

New Salicylanilide Derivatives and Their Peptide Conjugates as Anticancer Compounds: Synthesis, Characterization, and *In Vitro* Effect on Glioblastoma

Lilla Horváth,[#] Beáta Biri-Kovács,[#] Zsuzsa Baranyai, Bence Stipsicz, Előd Méhes, Bálint Jezsó, Martin Krátký, Jarmila Vinšová, and Szilvia Bősze*

Cite This: *ACS Omega* 2024, 9, 16927−16948

Read Online

ACCESS | Metrics & More | Article Recommendations | Supporting Information

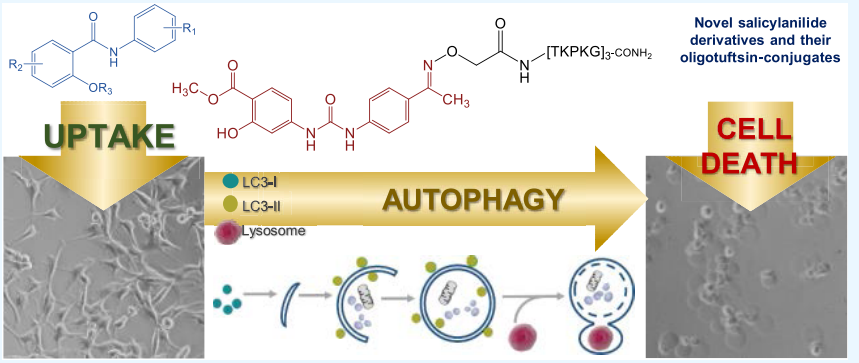

ABSTRACT: Pharmacologically active salicylanilides (2-hydroxy-*N*-phenylbenzamides) have been a promising area of interest in medicinal chemistry-related research for quite some time. This group of compounds has shown a wide spectrum of biological activities, including but not limited to anticancer effects. In this study, substituted salicylanilides were chosen to evaluate the *in vitro* activity on U87 human glioblastoma (GBM) cells. The parent salicylanilide, salicylanilide 5-chloropyrazinoates, a 4-aminosalicylic acid derivative, and the new salicylanilide 4-formylbenzoates were chemically and *in vitro* characterized. To enhance the internalization of the compounds, they were conjugated to delivery peptides with the formation of oxime bonds. Oligotuftsins ($[TKPKG]_n$, $n = 1-4$), the ligands of neuropilin receptors, were used as GBM-targeting carrier peptides. The *in vitro* cellular uptake, intracellular localization, and penetration ability on tissue-mimicking models of the fluorescent peptide derivatives were determined. The compounds and their peptide conjugates significantly decreased the viability of U87 glioma cells. Salicylanilide compound-induced GBM cell death was associated with activation of autophagy, as characterized by immunodetection of autophagy-related processing of light chain 3 protein.

INTRODUCTION

Glioblastoma (GBM) is the most aggressive and most prevalent form of malignant gliomas with a poor prognosis.[1−6] GBM is WHO grade IV glioma and is characterized by histopathological features such as cellular and nuclear atypia, poorly differentiated neoplastic astrocytes, brisk mitotic activity, diminished apoptosis, pseudopallisading necrosis, neo-angiogenesis, and vascular thrombosis. To distinguish GBM from lower-grade gliomas, vascular hyperproliferation and necrosis are essential diagnostic features.[2,3] Currently the Stupp protocol is applied to treat high-grade gliomas.[5−8] After surgical resection, 6 weeks of combined radio- and chemotherapy is applied, followed by chemotherapy alone. Temozolomide (TMZ), a DNA alkylating agent, is used for chemotherapy.[7]

Despite the progress in cancer treatments, almost no advancement in the therapy of gliomas has been introduced; those brain tumors display stemness signatures, and new strategies against the highly proliferative activity of glioma cells have been studied and new compounds acting against them are needed.[5,6] These new agents need to penetrate the blood−brain barrier, then also penetrate through the tissue of the whole brain, and selectively eliminate cancer cells without harming the normal brain tissue.[2,3] The malignant glioma resistance to chemotherapy[9,10] suggests that cancer therapy should include agents that target residual cells to prevent the regrowth of neoplastic cells.[11] Numerous molecular and

Received: August 4, 2023
Revised: December 28, 2023
Accepted: January 3, 2024
Published: April 5, 2024

© 2024 The Authors. Published by American Chemical Society

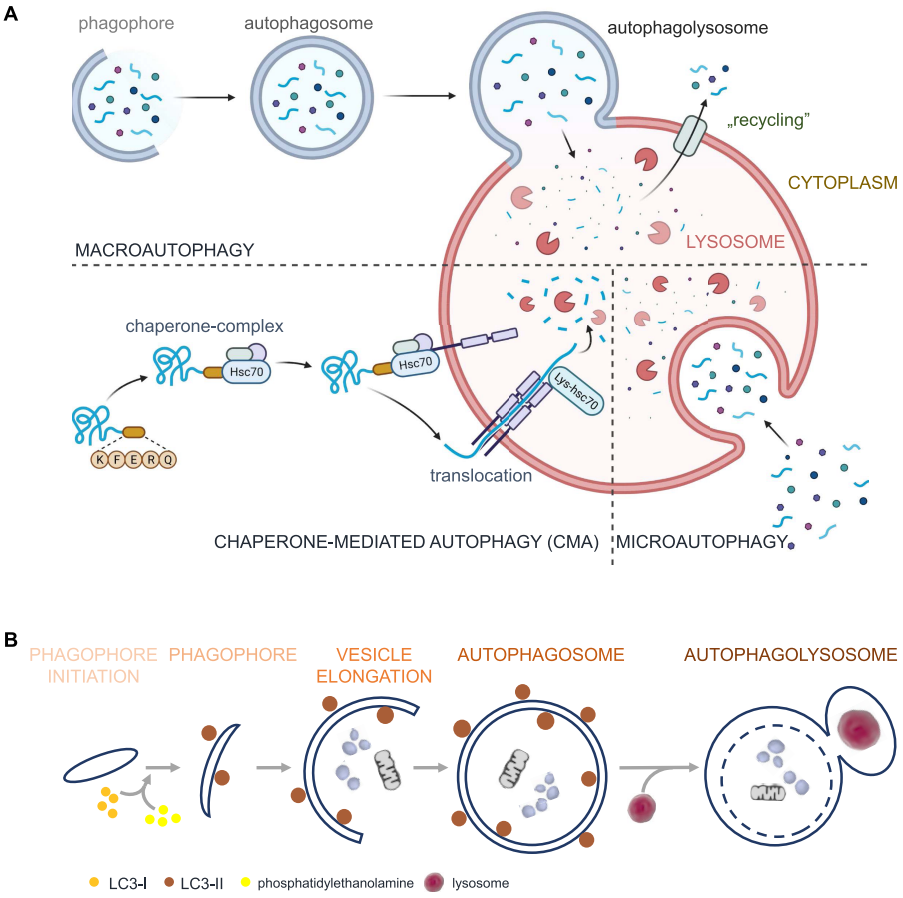

Figure 1. Autophagy is an intracellular degradation system. (A) Types of autophagic pathways. Microautophagy engulfs cytoplasmic cargo in the lysosome or vacuole membrane itself. CMA is the recognition, delivery, and translocation of target proteins from the cytoplasm to the lysosome lumen. Autophagosome formation is the hallmark of macroautophagy. (B) Process of macroautophagy. Vesicles derived from the endoplasmic reticulum form phagophore membranes. The phagophore elongation and sequestration are mediated by the phosphatidylethanolamine conjugate of LC3-I, LC3-II. The autophagosome is a double-membraned organelle. The autophagosome with the lysosome forms autophagolysosomes, where the degradation happens.

cellular targets are described as a possibility in GBM treatment,[12,13] and modulation of the autophagic flux is one of them.[14−19]

Autophagy is a complex process that is responsible for the intracellular delivery and degradation of cellular components. The three main autophagic routes, macroautophagy, microautophagy, and chaperone-mediated autophagy (CMA), are depicted in (Figure 1A).[20−23] Macroautophagy (from here, "autophagy") is mediated by the characteristic double-membraned organelles, autophagosomes.[20,21] Cellular stress, starvation, or tumor suppressors are activating the autophagy-related (Atg) protein cascade while suppressing the autophagy-inhibiting mammalian target of the rapamycin pathway. Thus, vesicles derived from the endoplasmatic reticulum are forming the phagophore membrane.[24] During the elongation of the phagophore, phosphatidylethanolamine is conjugated to the microtubule-associated protein 1A/1B-light chain 3 (LC3) LC3-I protein, forming LC3-II, which is built into the phagophore membrane. LC3-II is the most common autophagy marker.[25,26] As the phagophore grows, it engulfs cytoplasmic content which contains proteins or damaged organelles. The sequestration of the phagophore forms the autophagosome that delivers the cytoplasmic content to the lysosomes, and the coalescence of the two forms the autophagolysosomes, where the degradation happens (Figure 1B). After the degradation, the monomers and building blocks are recycled to the cytoplasm for further use.[20,21,26,27]

Autophagy modulators have a different effect on cancer progression depending on the type and status of the disease.[15,16,28−30] Autophagy can serve as an adaptive survival mechanism, and high-level autophagy can cause autophagy-mediated type II programmed cell death.[31,32] Supporting Information Table S1 summarizes the effect of autophagy modulators on brain cancer cell cultures. TMZ and bevacizumab, two clinically used antiglioblastoma agents, induce autophagy; however, blocking autophagy enhances the cytotoxic activity of these compounds.[33−35] Treatment of GBM stem cells with an oncogenic adenovirus (delta-24-RGD) resulted in autophagic cell death *in vitro* and *in vivo*.[36] The bioactive alkaloid of *Sinomenium acutum*, sinomenine hydrochloride, possesses its cytostatic, epithelial-to-mesenchymal transformation (EMT), and metastasis-suppressing effect *via* autophagy induction.[37] In the case of neuroblastoma cell cultures with 18α-glycyrrhetinic acid, a bioactive triterpenoid, autophagy activation has a pro-survival effect: autophagy inhibition enhanced apoptotic pathways.[38] Gambogic acid, a product derived from *Garcinia hanburyi*, induced protective autophagy in GBM cells.[39,40] Gintonin induced strong autophagy upregulation in primary cortical astrocytes.[41] The Src tyrosine kinase inhibitors, such as Si306 and pro-Si306,

https://doi.org/10.1021/acsomega.3c05727
ACS Omega 2024, 9, 16927−16948

Table 1. Autophagy-Modulating Salicylanilide and Other Derivatives

compound's trivial name	tumor model	compound's role in autophagy	autophagy marker	detection method	cell viability assay	refs
niclosamide[a]	cervical carcinoma: HeLa	induction of noncanonical LC3 lipidation	LC3, ATG5, ATG16L1, ATG12, WIPI2	WB, FM		76
		mitochondria fragmentation; enhancement of apoptotic and autophagic cell death	LC3, ATG5	WB, CLSM	MTT, CCK	79
	brain (GBM): U87, U118	induction of autophagy through activation of ER stress may initiate cell death	LC3, monodansyl-cadaverine	WB, CLSM	MTS	80
	colorectal cancer: U2OS, WIDR, DLD-1, CRC 240, COLO205, CRC57, HCT116	involvement of autophagosomes in niclosamide-mediated cancer cell growth inhibition	LC3, Beclin-1, ULK-1, phospho-ULK-1	WB, CLSM	MTS, caspase activity	81,82
	lung adenocarcinoma: A549, CL1−5	blocking autophagy improves the cytotoxic effect	LC3, ATG5, p62	WB, CLSM, IHC	MTT, FC (annexin V)	78
	pancreatic cancer: SW1990, COLO357, T3M4, CFPAC1, CD18/HPAF, BxPC-3, MIA PaCa, PANC-1, AsPC-1, Capan-1	autophagy activation via mitochondrial stress and the mTORC-1 pathway results in cell death and increased crosstalk between autophagy and apoptosis	LC3, Beclin-1, p62	WB, CLSM	MTT, calcein AM, colony-forming assay	83
	cervical carcinoma: HeLa	induction of autophagy by suppression of mTOR activity	LC3, ATG12, MAP1LC3, p62, ATG16L1 puncta-tion	WB, FM		75
	lung adenocarcinoma: A549					
	breast adenocarcinoma: MCF-7	stimulation of autophagy and inhibition of mTORC1 signaling	LC3	WB, CLSM, au-tomated mi-croscopy	MTT, FC (annexin V)	77
perhexiline[b]						
amiodarone[c]						
rottlerin[d]						
LCC09[e]	GBM: U87, D54	mTOR suppression	mTOR, Akt	WB	MTT	90
LCC03[f]	castration-resistant prostate cancer: PC3, DU145, C4−2, CWR22Rv1	autophagy induction via the canonical and noncanonical pathways results in cytotoxicity	LC3, Beclin-1, ATG12	WB, CLSM, TEM	WST-1 kit	91
6k[g]	chronic myelogenous leukemia: K562	promotion autophagy leading to cell death executed by caspases	LC3	WB	calcein AM	92
	breast adenocarcinoma: MCF-7					
	brain (GBM): G361					
	melanoma: A-375, IPC-298, Sk-Mel-30	disruption of the actin cytoskeleton inducing pro-survival autophagy	LC3	WB, CLSM	WST-1 kit, PI exclu-sion, FC (annexin V)	93
rafoxanide[h]	gastric cancer: SGC-7901, BGC-823	inhibition of autophagy attenuating rafoxanide-induced apoptosis	LC3	WB, CLSM	CCK, FC (annexin V)	89
	colorectal cancer: HCT-116, DLD1	induction of autophagy and immunogenic cell death	LC3	WB	FC (annexin V)	94

[a][5-Chloro-*N*-(2-chloro-4-nitrophenyl)-2-hydroxybenzamide]. [b][2-(2,2-Dicyclohexylethyl)piperidine]. [c]({2-[4-(2-Butyl-1-benzofuran-3-carbonyl)-2,6-diiodophenoxy]ethyl}diethylamine). [d]((2*E*)-1-{6-[(3-Acetyl-2,4,6-trihydroxy-5-methylphenyl)methyl]-5,7-dihydroxy-2,2-dimethyl-2*H*-chromen-8-yl}-3-phenylprop-2-en-1-one). [e][*N*-(3-Cyanophenyl)-2′,4′-difluoro-4-hydroxy-(1,1′-biphenyl)-3-carbox-amide]. [f][*N*-(3,4-Difluorophenyl)-2′,4′-difluoro-4-hydroxy-(1,1′-biphenyl)-3-carboxamide]. [g]((*R*)-5-Chloro-*N*-{1-[(4-chlorophenyl)amino]-1-(oxo)-3-phenylpropan-2-yl}-2-hydroxybenzamide). [h]{*N*-[3-Chloro-4-(4-chlorophenoxy)phenyl]-2-hydroxy-3,5-diiodobenzamide}; WB: Western blot, CLSM: confocal laser scanning microscopy, IHC: immunohistochemistry, TEM: transmission electron microscopy, FC: flow cytometry, FM: fluorescence microscopy, and CCK: cell counting kit 8.

https://doi.org/10.1021/acsomega.3c05727
ACS Omega 2024, 9, 16927−16948

induce autophagy in GBM cells. Bafilomycin A1 enhances the cytotoxic effect of the compounds while inhibiting autophagic flux within the cell, suggesting the cytoprotective role of autophagy after the treatment with Si306 or pro-Si306.[42] Salicylanilides (2-hydroxy-*N*-phenylbenzamides) exhibit a wide spectrum of activities; therefore, they are a subject of interest in medicinal chemistry.[43−59] They have antitumor,[60] antibacterial,[61−64] antifungal,[65] antiviral,[66,67] and anthelmintic[68] activities. Table 1 summarizes the autophagy-modulating salicylanilide derivatives with antitumor activity. The trivial and IUPAC names, CAS numbers, and structures of these compounds are summarized in Supporting Information Table S2. Niclosamide, an orally administered broad-spectrum anthelmintic salicylanilide,[68] has an anticancer effect against several malignancies.[69−74] Niclosamide induces autophagy in cancer cells[75−77] which have pro-survival roles in lung adenocarcinoma cells.[78] In contrast, niclosamide-induced autophagy resulted in cell death of cervical carcinoma,[79] GBM,[80] colorectal cancer,[81,82] and pancreatic cancer[83] cells. Niclosamide selectively inhibited GBM cells; it has pro-apoptotic, antiproliferative, and antimigratory effects in primary human glioblastoma cells (pGBMs). Survival of xenografted mice after exposure to pGBMs significantly increased due to niclosamide. Analysis of the mechanism revealed that niclosamide inhibited intracellular WNT/CTNNB1-, NOTCH-, mTOR-, and NF-kB signaling cascades simultaneously.[84] Niclosamide in combination with TMZ (the first-line drug for GBM) showed a synergistic anticancer effect on glioma cells with NFKBIA deletion.[84] The inhibition of NF-kB activity could be utilized to overcome the resistance to TMZ,[85] at least in NFKBIA ± GBM genotypes.[84] In a recent study Mito et al. designed and synthesized niclosamide derivatives to define structure−activity relations on U87 human GBM cells.[86]

Novel salicylanilide derivatives were identified with antiproliferative effects against human cancer cell lines (pulmonary carcinoma cell line A549 and squamous cell carcinoma cell line A431) that overexpress EGFR.[87] A salicylanilide derivative [*N*-(4-ethoxyphenyl)-2-hydroxybenzoic-acid amide, SUCI02, efuamide] reportedly inhibits phosphorylation and signaling of erbB-2 tyrosine kinase receptor, resulting in cell cycle blockage in breast cancer cells.[88] Salicylanilide derivatives can also induce autophagy (Table 1), which resulted in cell death of gastric cancer,[89] GBM,[90] and castration-resistant prostate cancer[91] cell cultures. (*R*)-5-Chloro-*N*-{1-[(4-chlorophenyl)-amino]-1-oxo-3-phenylpropan-2-yl}-2-hydroxybenzamide, 6k, a substituted 2-hydroxy-*N*-(arylalkyl)benzamide, promoted cell death via autophagy in chronic myelogenous leukemia, breast adenocarcinoma, and GBM cells;[92] however, in melanoma cell lines, the pro-survival role of 6k-induced autophagy was determined.[93]

The selectivity of the compounds can be increased by applying different targeting systems. As a molecular target, neuropilin receptors (NRPs) can be used in different types of cancer,[95−99] including GBM.[100−107] NRPs are involved in many biological processes including axonal guidance, angiogenesis, and lymphangiogenesis.[108] In cancer biology, NRPs are associated with tumor angiogenesis,[97,99] cell proliferation, migration, metastasis,[109] EMT, and maintaining immature phenotype.[96] NRP expression is upregulated in glioma tissue, and increased expression is concurrent with the elevation of the glioma grade and is linked with poor prognosis.[100] The role of NRP signaling in tumor aggressiveness has been also described.[106] Thus, targeting NRPs in GBM is a possible way to increase compound selectivity. Several carrier peptides have been applied to target moieties against GBM.[60,107] Tuftsin (human: TKPR, canine: TKPK) is a natural peptide ligand of NRPs[110] with several biological effects including immunostimulatory and anticancer activities.[111−115] In this study, oligotuftsin derivatives (OT5, OT10, OT15, OT20 = $[TKPKG]_{1-4}$)[116] were used as a peptide carrier. To compare the internalization of the tuftsin derivatives, the UC_{50} values (this is the interpolated concentration which is required for the fluorescence signal coming from 50% of the measured cells) were calculated.[117]

In this paper, we describe promising and effective substituted salicylanilide derivatives against GBM. Temporarily masking the hydroxy group of salicylanilides can result in improved physicochemical properties, which leads to better internalization ability, bioavailability, and higher activity.[62,118−120] Therefore, in this study, salicylanilide derivatives and their tuftsin conjugates were chosen to evaluate the *in vitro* activity on a GBM cell culture.

MATERIALS AND METHODS

Materials. All materials (commercial-grade; all reagents and solvents were of analytical grade or the highest available purity and were used without further purification) for the synthesis of salicylanilide compounds were purchased from Sigma-Aldrich and Merck (Darmstadt, Germany).

For peptide synthesis, Fmoc-Rink Amide MBHA resin, amino acid derivatives, and Boc-aminooxyacetic acid (Boc-Aoa−OH) were produced by Iris Biotech GmBH (Marktredwitz, Germany). *N*,*N*-diisopropylethylamine (DIEA) was from Fluka (Charlotte, NC, USA). 1-Methyl-2-pyrrolidone (NMP), piperidine, 1,8-diazabicyclo[5.4.0]undec-7-ene (DBU), 1-hydroxybenzotriazole (HOBt), *N*,*N*′-diisopropylcarbodiimide (DIC), triisopropylsilane (TIS), acetic anhydride, ethylene glycol monoethyl ether, 5(6)-carboxyfluorescein (Cf), and methanol were from Sigma-Aldrich (Budapest, Hungary). Trifluoroacetic acid (TFA), *N*,*N*-dimethylformamide (DMF), diethyl ether, and acetonitrile were from VWR (VWR International, Debrecen, Hungary). Ninhydrin, isatin, acetic acid, and dimethyl sulfoxide (DMSO) were from Reanal Laboratory Chemicals (Budapest, Hungary).

For the *in vitro* experiments, nonessential amino acids, fetal bovine serum (FBS), and penicillin/streptomycin (10 000 units penicillin/10 mg streptomycin/mL) were procured from Gibco (Thermo Fisher Scientific, Waltham, MA, USA). Dulbecco's modified Eagle's medium (DMEM), EGM-2 endothelial cell growth medium (CC-3162), phosphate buffered saline (PBS), L-glutamine, pyruvate, and trypsin were procured from Lonza (Basel, Switzerland). 3-(4,5-Dimethylthiazol-2-yl)-2,5-diphenyltetrazolium bromide (MTT), ethylenediaminetetraacetic acid (EDTA), paraformaldehyde (PFA), Mowiol 4−88, and HPMI buffer were prepared in our laboratory using components [NaCl, *N*-(2-hydroxyethyl)piperazine-*N*′-(2-ethanesulfonic acid)—HEPES, glucose, $NaHCO_3$, KCl, $MgCl_2$, $CaCl_2$, and $Na_2HPO_4 \times 2H_2O$); mounting medium (Prolong Glass Antifade Mountant with NucBlue Stain, P36981), polyclonal *anti-β*-catenin antibody (A31572, produced in rabbit), and ZO-1 (rabbit, polyclonal, SAB3500301) were purchased from Sigma-Aldrich (Budapest). Antirabbit Ig-Alexa555 (C2206, produced in donkey) and antimouse-horseradish peroxidase (HRP) secondary antibody (32430, produced in goat) were procured from

https://doi.org/10.1021/acsomega.3c05727
ACS Omega 2024, 9, 16927−16948

Invitrogen (Thermo Fisher Scientific, Waltham, MA, USA). All buffers used during the Western blot technique were made in-house using components obtained from VWR or AppliChem GmbH (Darmstadt, Germany). Acrylamide and *N*,*N*′-methylenebis(acrylamide) were obtained from Serva Electrophoresis GmbH (Heidelberg, Germany). Anti-LC3I/II antibody (12471, rabbit) was purchased from Cell Signaling Technology (Danvers, MA, USA). Antineuropilin-1 (sc-5307, produced in mouse), antineuropilin-2 (sc-13117, produced in mouse), and antiactin (sc-1616, produced in goat) primary antibodies and antirabbit-horseradish peroxidase (HRP) (sc-2004, produced in goat, 1:2000) and antigoat-HRP (sc-2354, produced in mouse) secondary antibodies were procured from Santa Cruz Biotechnology (Dallas, TA, USA). Antimouse-HRP secondary antibody (32430, goat), LysoTracker Deep Red (L12492), Hoechst 33342 (62249), and CellTracker Green Dye (CMFDA, C7025, 5-chloromethylfluorescein diacetate) were obtained from Invitrogen Biotechnology (Thermo Fisher Scientific, Waltham, MA, USA).

Chemistry. *General Methods.* Reactions were monitored using thin-layer chromatography. Plates coated with 0.2 mm silica gel 60 F254 (Merck) were used, and the spots were visualized using UV irradiation (λ = 254 nm). All melting points were determined by a Melting Point apparatus B-540 (Büchi) using open capillaries, and the melting point values were uncorrected. Infrared spectra (KBr pellets) were recorded using an FT-IR spectrometer (Nicolet 6700 FT-IR; Thermo Fisher Scientific, Waltham, MA, USA) using a range of 400−4000 cm^{-1} with the ATR technique. The NMR spectra were measured at ambient temperature on a Varian Mercury-Vxbb 300 (300 MHz for ^1H and 75.5 MHz for ^{13}C; Varian Comp., Palo Alto, CA, USA) or a Varian VNMR S500 instrument (500 MHz for ^1H and 126 MHz for ^{13}C; Varian Comp., Palo Alto, CA, USA) using deuterated dimethyl sulfoxide (DMSO-d_6; for salicylanilides) or $CDCl_3$ (for esters) solutions of the samples. The chemical shifts, δ, are given in ppm in relation to tetramethylsilane as an internal standard. The coupling constants (J) are presented in Hz. Elemental analysis (C, H, N) was performed using an automatic microanalyzer (CHNS−O CE; FISONS EA 1110, Milano, Italy). Monoisotopic molecular mass was acquired by a Bruker Esquire 3000+ ESI-MS (Bruker Corporation, Billercia, MA, USA). Samples were dissolved in a solution of acetonitrile/water = 1/1 (v/v) containing 0.1% acetic acid that was injected by a syringe pump with a flow rate of 10 μL/min. Data was evaluated using Bruker DataAnalysis software (Bruker Corporation). For high-resolution mass spectrometry, a Q Exactive Focus Hybrid Quadrupole-Orbitrap Mass Spectrometer (Thermo Fisher Scientific, Bremen, Germany) was used (flow rate: 3.0 μL/min). Data was evaluated using Thermo Scientific Xcalibur software (Thermo Fisher Scientific).

Synthesis of the Peptide Carriers and Conjugation with Oxime Bond Formation. Carrier peptides (OT5: TKPKG, OT10: $[TKPKG]_2$, OT15: $[TKPKG]_3$, and OT20: $[TKPKG]_4$) were synthesized using the Fmoc/^{t}Bu strategy based on the work of Baranyai et al.[121] Briefly, the peptides were built manually on Fmoc-Rink Amide MBHA resin (loading: 0.69 mmol/g). One cycle of the synthesis followed this protocol: (i) Fmoc cleavage: 2% piperidine and 2% DBU in DMF (v/v), 2, 2, 5, and 10 min, (ii) washing the resin with DMF, 5 × 1 min, (iii) ninhydrin or isatin test, (iv) coupling: 3 equiv Fmoc-amino acid derivative/DIC/HOBt dissolved in NMP, 60 min, (v) washing the resin with DMF, 5 × 1 min, (vi) ninhydrin or isatin test, and (vii) recoupling if necessary. After the completion of the sequence, peptide resin was divided for the synthesis of acetylated (Ac-), 5(6)-carboxyfluorescein (Cf-), and (aminooxy)acetylated (Aoa-) derivatives. Peptide derivatives were cleaved from the resin using TFA, with the addition of appropriate scavengers (H_2O, TIS, 2.5 h). After filtration, the peptide content was precipitated in ice-cold diethyl-ether, centrifuged, freeze-dried in water, and stored at 4 °C. Crude products were purified using a RP-HPLC system (Knauer, Bad Homburg, Germany) on a Phenomenex Jupiter C_{18} column (10 μm, 90 Å, 10 × 250 mm, Torrance, CA, USA).

An oxime bond was formed between the carbonyl group of SalBenz-1 or ASA1 and the Aoa-peptide derivatives based on Baranyai et al.[121] SalBenz-1 was dissolved in DMF, ASA1 was dissolved in ethylene glycol monoethyl ether, and Aoa-peptides were dissolved in 0.2 M sodium acetate−acetic acid buffer (pH ∼ 4.9). After the two solutions were mixed in a molar ratio of 1:1, the reaction mixtures were acidified using acetic acid. Conjugations were monitored using an Exformma analytical RP-HPLC system (Exformma Technology, ASIA Co., Limited, Hong Kong, China) with an Agilent Zorbax SB-C_{18} column (5 μm, 100 Å, 4,6 mm × 150 mm, Santa Clara, CA, USA) or a YMC-Pack ODS-A C_{18} column (100 Å, 4.6 × 150 mm, Kyoto, Japan). Eluent A was 0.1% (v/v) TFA in water and eluent B was 0.1% (v/v) TFA in acetonitrile/water = 80:20 (v/v). The gradient was 0−5 min 0% B, 5−15 min 0−60% B, and 15−25 min 60−100% B, with a flow rate of 1 mL/min and a detector wavelength λ of 220 nm. Products were purified using a Knauer semipreparative RP-HPLC system on a Phenomenex Jupiter C_{18} column.

Chemical Characterization of the Conjugates. The homogeneity of the compounds was checked by the system described earlier in "Synthesis of the Peptide Carriers and Conjugation with Oxime Bond Formation". The column, gradient, and composition of the eluents are also described above.

The mass accuracy of the peptide derivatives and conjugates was determined with the help of a Q Exactive Focus Hybrid Quadrupole-Orbitrap Mass Spectrometer (Thermo Fisher Scientific). Distilled water and acetonitrile = 1:1 (v/v) with 0.1% formic acid solution was used to dissolve the samples. Mass spectra were recorded in the positive mode and the target mass range was 200−2000 m/z with a flow rate of 3.0 μL/min. Thermo Scientific Xcalibur software was used to graph and evaluate the mass spectra.

Synthesis of Salicylanilide Derivatives. Synthesis and characterization of Sal, SalPyr-1, SalPyr-2, SalPyr-7, and ASA1 were previously published.[61,62,64,122] For detailed information, see the Supporting Information section Synthesis of salicylanilide derivatives (pages S15−16).

The synthesis of the new salicylanilide esters SalBenz-1 and SalBenz-2 was carried out by using 4-formylbenzoic dissolved in dry *N*,*N*-dimethylformamide (10 mL). Then the appropriate salicylanilide (both 1 mmol) was added, and the solution was then cooled to −20 °C, and a mild excess of *N*,*N*′-dicyclohexylcarbodiimide (DCC, 1.2 mmol) was added in three portions for 1 h. The solution was then stirred for 3 h and maintained at the same temperature and then later stored at +4 °C for 20 h. After the precipitated byproduct *N*,*N*′-dicyclohexylurea was filtered off, the solvent was evaporated using vacuum. The remainder was dissolved using a small amount of ethyl acetate, with the insoluble portion being

https://doi.org/10.1021/acsomega.3c05727
ACS Omega 2024, 9, 16927−16948

filtered off. To initiate crystallization, the filtrate was partially evaporated. The mixture was then stored for 12 h at +4 °C. To yield the crude benzoates, the precipitate was filtered out. By crystallization from acetone-hexane, the product was purified.

4-Chloro-2-{[4-(trifluoromethyl)phenyl]carbamoyl}phenyl 4-Formylbenzoate (SalBenz-1). White solid; yield 71%; mp 201.0−203.0 °C. IR (ATR): 3384, 3105, 2848, 1740 (CO ester), 1690 (CO), 1603, 1530, 1480, 1411, 1341, 1319, 1276, 1252, 1212, 1166, 1109, 1091, 1066, 1015, 852, 839, 819, 750, 679. ^{1}H NMR (300 MHz, DMSO-d_6): δ 10.90 (1H, s, NH), 10.11 (1H, s, CO−H), 8.25 (2H, d, J = 8.2 Hz, H2″, H6″), 8.05 (2H, d, J = 8.2 Hz, H3″, H5″), 7.89 (1H, d, J = 2.6 Hz, H3), 7.83 (2H, d, J = 8.5 Hz, H3′, H5′), 7.75 (1H, dd, J = 8.7 Hz, J = 2.6 Hz, H5), 7.64 (2H, d, J = 8.5 Hz, H2′, H6′), 7.55 (1H, d, J = 8.7 Hz, H6). ^{13}C NMR (75 MHz, DMSO-d_6): δ 193.03, 163.68, 163.14, 146.98, 142.43, 139.79, 133.31, 131.97, 130.80, 130.68, 130.63, 129.90, 129.27, 126.22 (q, J = 3.7 Hz), 125.63, 124.50 (q, J = 270.9 Hz), 124.10 (q, J = 31.8 Hz), 122.64, 119.91. $MS_{monoizotopic}$ (calc/meas): 447.0/447.1. Anal. Calcd for $C_{22}H_{13}BrClF_3NO_4$ (447.79): C, 59.01; H, 2.93; N, 3.13. Found: C, 59.31; H, 2.64; N, 3.00.

4-Chloro-2-[(3,4-dichlorophenyl)carbamoyl]phenyl 4-Formylbenzoate (SalBenz-2). White solid; yield 59%; mp 228.5−230.0 °C. IR (ATR): 3365, 3095, 2842, 1736 (CO ester), 1688 (CO), 1597, 1528, 1479, 1377, 1311, 1277, 1241, 1207, 1142, 1107, 1092, 1014, 843, 833, 819, 751, 682. ^{1}H NMR (500 MHz, DMSO-d_6): δ 10.80 (1H, s, NH), 10.12 (1H, s, CO−H), 8.25 (2H, d, J = 7.9 Hz, H2″, H6″), 8.06 (2H, d, J = 8.0 Hz, H3″, H5″), 7.91 (1H, s, H2′), 7.88 (1H, d, J = 2.6 Hz, H3), 7.75 (1H, dd, J = 8.7 Hz, J = 2.6 Hz, H5), 7.59−7.50 (3H, m, H6, H5′, H6′). ^{13}C NMR (126 MHz, DMSO-d_6): δ 193.04, 163.64, 162.95, 146.95, 139.80, 138.88, 133.27, 132.03, 131.83, 131.08, 130.85, 130.68, 130.63, 129.89, 129.23, 125.68, 125.63, 121.17, 120.03. $MS_{monoizotopic}$ (calc/meas): 447.9/447.2. Anal. Calcd for $C_{21}H_{12}Cl_3NO_4$ (448.68): C, 56.21; H, 2.70; N, 3.12. Found: C, 56.50; H, 3.02; N, 2.87.

Stability Study of the Salicylanilide Derivatives. Monitoring the stability of the parent salicylanilide (Sal), a salicylanilide 4-formylbenzoate (SalBenz-1), the 4-aminosalicylic acid derivative (ASA1), and a salicylanilide 5-chloropyrazinoate (SalPyr-1) was carried out using analytical RP-HPLC by an Exformma HPLC system with a Nucleosil C_{18} HPLC Column (5 μm 4.6 mm × 150 mm, 100 Å, Sigma-Aldrich, Budapest). The eluents, gradient, and flow rate are described in the section "Synthesis of the Peptide Carriers and Conjugation with Oxime Bond Formation". The detection was carried out at λ = 280 nm.

The purified fractions were freeze-dried and also characterized using mass spectrometry with the help of ESI-MS (data not shown). With the help of a Bruker Daltonics Esquire 3000+, positive and negative electrospray ionization mass spectrometric analysis was performed. The samples were dissolved in acetonitrile−water solution (50:50, v/v) containing 0.1% acetic acid.

Since DMSO stock solution was used in the *in vitro* studies, the chemical stability of the compounds was studied in DMSO (c = 0.5 mg/mL) and also in serum-free RPMI-1640 medium containing 10% DMSO (c = 0.5 mg/mL). In the *in vitro* experiments, serum-free RPMI-1640 medium containing 1% DMSO was used, but the RP-HPLC studies required a higher concentration and, because of the moderate solubility of the compounds in the medium, the percentage of DMSO needed to be increased to 10%.

Characterization of the Compounds Using the Chemicalize Online Platform. To determine whether the compounds fulfill the criteria of Lipinski's rule of five, a chemical characterization using the Chemicalize (https://chemicalize.com/) online platform was performed. The log P values, solubility characteristics (including intrinsic solubility), molecular weight, number of hydrogen bond donors and acceptors, and molar refractivity data were calculated.

***In Vitro* Characterization.** *Cell Culturing and Maintenance.* U87 human GBM cells (ATCC HTB-14, RRID CVCL_0022)[123] were maintained in DMEM [with 10% FBS, 2 mM L-glutamine, 1% nonessential amino acids, 1 mM sodium pyruvate and 1% penicillin−streptomycin antibiotics (complete medium, CM)]. Human umbilical vein endothelial cells (HUVEC, CC-2519A, Lonza) were kept in EGM-2 endothelial cell growth medium (CC-3162, Lonza) containing penicillin-streptomycin-amphotericinB (17−745E, Lonza). Both cell cultures were maintained at 37 °C in a 5% CO_2 atmosphere.

In Vitro Internalization Studies. U87 or HUVEC cells were plated (10^5 cells/1000 μL CM/well, 1 day before the assay, 24-well plate). The treatment lasted for 90 min, 3 h, or 24 h with the Cf-peptides dissolved in serum-free medium (ICM) (c_{DMSO} = 1.0 v/v %) at the 3.125−50 μM concentration range. Treatment of the control cells was done with ICM only or with DMSO containing ICM (c = 1.0%, v/v) at 37 °C. After incubation and treatment, cells were washed using ICM and with HPMI buffer (9 mM glucose, 10 mM $NaHCO_3$, 119 mM NaCl, 9 mM HEPES, 5 mM KCl, 0.85 mM $MgCl_2$, 0.053 mM $CaCl_2$, and 5 mM $Na_2HPO_4 \times 2H_2O$, pH 7.4).[124] Once the washing steps were complete, 100 μL trypsin was added to the cells for 5 min. Trypsin activity was stopped using HPMI augmented with 10% FBS. Cells were then transferred into FACS tubes (Sarstedt) and centrifuged (1000 rpm, 5 min) and, after removing the supernatant, a further 250 μL of HPMI was added to the cells. For the internalization studies, a BD LSR II flow cytometer (BD Biosciences, San Jose, CA, USA) was used. Cells were first gated on size and granularity (SSC *vs* FSC), and then live cells were gated by using propidium iodide (10 μg/mL) (PI) solution. Intracellular fluorescence intensity was measured at λ_{ex} = 488 nm (Coherent Sapphire laser excitation, emission channel—LP 510, BP 530/30; FITC-channel). To identify the internalization of Cf-peptides, live cells were divided into FITC-positive (Cf-positive) and FITC-negative (Cf-negative) subpopulations. To analyze the results, FACSDiva 5.0 software was used. All measurements were performed in duplicate.

Confocal Laser Scanning Microscopy. Imaging of Cf-peptide derivatives was carried out using a Zeiss LSM 710 confocal laser scanning microscope (Carl Zeiss Microscopy GmbH, Jena, Germany). U87 cells were seeded onto microscopy coverslips (#1, diameter: 13 mm, Thermo Fisher Scientific) and placed in 24-well cell culture plates (85,000 cells/500 μL of medium/well) 1 day before the assay. Cf-peptides (25 μM, in DMEM ICM) were added to the cells using 3 h of incubation time. After washing with ICM, cells were incubated with LysoTracker Deep Red (30 min, 80 nM, in ICM) for visualization of lysosomes. Nuclei were labeled with Hoechst 33342 (10 min, 0.2 μM). 4% PFA was used for fixation (20 min, at 37 °C). After washing with PBS, coverslips were mounted on slides using Mowiol 4−88. The imaging was carried out using the Zeiss LSM 710 system with a 40× oil objective with the following parameters: Cf-peptides λ_{ex} = 488

https://doi.org/10.1021/acsomega.3c05727
ACS Omega 2024, 9, 16927−16948

nm and λ_{em} = 541 nm, nuclei λ_{ex} = 405 nm and λ_{em} = 467 nm (Hoechst 33342), and lysosomes λ_{ex} = 633 nm and λ_{em} = 720 nm (LysoTracker Deep Red). Images were processed using Zeiss ZEN lite software (Carl Zeiss Microscopy GmbH).

Analysis of In Vitro Cytostatic Activity. Cells were plated onto 96-well plates 1 day before treatment (5000 cells/100 μL of medium/well). After 24 h of incubation at 37 °C, U87 cells were treated for 20−24 h with the compounds dissolved in ICM (c_{DMSO} = 1.0%, v/v) at 8 × 10^{-2} to the 100 μM concentration range. Control cells were treated with ICM only or with DMSO containing ICM (c = 1.0%, v/v) at 37 °C. After the treatment and incubation, cells were washed twice with ICM (centrifugation: 1000 rpm, 5 min), and then the cells were further incubated in ICM for 48 or 72 h. After incubation, the cell viability was determined with MTT-assay. 45 μL of MTT solution (2 mg/mL) was added to each well. Incubation time was 3.5 h; after that, cells were centrifuged (5 min, 2000 rpm) and the supernatant was removed, the crystals were dissolved in DMSO, and the optical density was determined at λ = 540 and 620 nm (ELISA Reader, Labsystems MS reader, Helsinki, Finland). OD_{620} was subtracted from OD_{540}. The percentage of cytostasis was calculated as (%) = 100 × (1 − $OD_{treated}/OD_{control}$), where $OD_{treated}$ and $OD_{control}$ correspond to the optical densities of treated and control cells, respectively. Cytostasis (%) was plotted as a function of concentration (logarithmic scale) and fitted to a sigmoidal curve, and the 50% inhibitory concentration (IC_{50}) value was determined from the curves using Microcal Origin (version 2018) software. Each experiment was repeated 2−3 times with 4−8 parallel measurements.

Western Blot Analysis. We applied Western blot analysis to (1) detect the NRPs on U87 cells and (2) examine the compounds' effect on autophagy. For the NRP detection, we applied the same method as described in ref 64. We prepared whole-cell protein extract of U87 cells in a lysis buffer containing 50 mM Tris (pH 7.4), 150 mM NaCl, 1% Triton-X 100, 2 mM EDTA, and the Halt Protease Inhibitor Cocktail (100×, Thermo Fischer Scientific). We ran equal amount of proteins on 10% Tris-tricine gel,[125] and next, we blotted in a Towbin buffer (pH ∼ 8.3) with 350 mA current for 45 min to a polyvinylidene fluoride (PVDF) membrane using the Bio-Rad Wet Blotting System (Bio-Rad Hungary, Budapest, Hungary). We used 4% milk powder in TBS-Tween buffer (pH ∼ 7.4) for blocking. NRPs were detected by an *anti*-NRP-1 or *anti*-NRP-2 antibody (1:80) followed by the antimouse-HRP secondary antibody (1:500). For the loading control, we used β-actin, detected by an antiactin antibody (1:2000), followed by the antigoat-HRP secondary antibody (1:2000). Finally, an enhanced chemiluminescence (ECL) substrate was added (SuperSignal West Pico PLUS Chemiluminescent Substrate, from Thermo Fisher Scientific), and we detected the chemiluminescent signal using the ChemiDoc XRS + Detection System (Bio-Rad Hungary).

To determine the compounds' effect on autophagy, U87 cells were treated with the compounds (10 μM), the conjugates (50 μM), or solvent (1% DMSO) in DMEM ICM for 24 h. After treatment, we washed the cells once with PBS. Next, cells were lysed in lysis buffer. We determined the protein concentration of samples using the Qubit Protein Assay Kit (Thermo Fischer Scientific). We ran an equal amount of proteins on 15% Tris-tricine gel and then blotted in the Towbin buffer (pH ∼ 8.3) with 350 mA current for 40 min to a PVDF membrane. After the blocking and washing steps, we detected the LC3 I/II proteins by an anti-LC3I/II antibody (1:1500) followed by an antirabbit-HRP secondary antibody (1:2000). We detected the chemiluminescent signal using the ChemiDocXRS + Detection System (Bio-Rad Hungary). Densitometry analysis of the Western blot measurements of the LC3 autophagy marker was performed using Bio-Rad ImageLab software. First, the bands were selected with the lane and bands tool. A background correction was performed using the lane profile tool. The density of the selected and background-corrected bands was calculated using the analysis tool. The densities were plotted using Microcal Origin software.

In Vitro Penetration of Cf-Tuftsin Peptides on the HUVEC-U87 Barrier Model. In preliminary experiments, we have tested different Transwell inserts [(TW), pore sizes and seeding procedures etc.; as described earlier[60,64]]. In this study, we used TW inserts of 0.4 μm pore size for the HUVEC barrier seeding. Prior to seeding, the polycarbonate microporous membrane of the inserts was equilibrated with CM EGM-2 (growth area: 0.412 cm^2). On the first day, 500 μL of HUVEC suspension in CM EGM-2 (8.5 × 10^4 cells) was pipetted onto the apical chamber and 2000 μL CM EGM-2 was added to the basolateral side. On days three and five, the CM EGM-2 was changed and the HUVEC monolayer was grown to confluence (the confluency was checked before and after the transport measurements).

The confluence of the HUVEC monolayer was monitored with CellTracker Green Dye (CMFDA, C7025, 5-chloromethylfluorescein diacetate). CellTracker Green Dye was dissolved in CM EGM-2 to reach 5 μM concentration. Following an incubation time of 15−45 min, the cells were washed with CM EGM-2. After stable green fluorescence developed, we imaged the cells *in situ*. We performed the image acquisition using a Zeiss Axio Observer Z1 inverted fluorescent microscope using either a 5× EC Plan-Neofluar objective or 10× Plan-Neofluar or 40× EC Plan-Neofluar objectives and a Zeiss Colibri illumination system with 365 nm, 470 nm, and 555 nm LED modules and a Zeiss HE25 filter set. The microscope was equipped with a Marzhauser SCAN-IM powered stage and a Zeiss AxioCam MRm CCD camera. For stage positioning and focusing as well as for acquisition of multifield mosaic images, we used Zeiss Axiovision 4.8 software. Finally, we processed the images using National Institute of Health (NIH) ImageJ software.

The tight junction and adherens junctions were also checked on the confluent monolayers. ZO1 and β-catenin were immunolabeled. ZO-1 is a prominent marker of the tight junction structures. It anchors tight junction proteins, such as claudins and occludins, to the actin cytoskeleton.[126] We applied the method described earlier.[64,127] Located in adherens junctions, β-catenin plays an important role in cell−cell adhesion by binding the cytoplasmic domains of cadherin-type adhesion molecules and thereby anchoring them to the actin cytoskeleton.[128]

Briefly, we fixed the cells on the TW membranes with 4% PFA in PBS and then treated them with 0.1% Triton X-100 in PBS. For blocking nonspecific binding sites, we used 1% bovine serum albumin in PBS. We used a polyclonal antibeta-catenin antibody (rabbit, Sigma—C2206, 1:100) for immunodetecting β-catenin, followed by an antirabbit Ig-Alexa555 secondary antibody (Invitrogen—A31572, 1:200). Finally, we excised the TW membranes and mounted them on glass slides (Thermo Scientific) using the ProLong mounting medium

https://doi.org/10.1021/acsomega.3c05727
ACS Omega 2024, 9, 16927−16948

Table 2. Characterization of the Peptide Derivatives

code	$Mw_{av(calc)}$[a]	$Mw_{mono(calc)}$[a]	measured m/z[b]	calculated m/z[c]	ppm[d]	R_t (min)[e]
Ac-OT20	2105.5270	2104.2844	527.0777	527.0784	−1.3	10.3
Cf-OT5[f]	886.9460	886.3861	444.2003	444.2003	0.0	12.9
Cf-OT10[f]	1398.5609	1397.6980	466.9066	466.9066	0.0	12.2
Cf-OT15	1910.1758	1909.0098	637.3438	637.3439	−0.1	12.3
Cf-OT20	2421.7908	2420.3216	346.7674	346.7675	−0.3	11.7

[a]Average and monoisotopic masses were calculated using CS ChemOffice Pro ver. 12.0. [b]Q Exactive Focus Hybrid Quadrupole-Orbitrap Mass Spectrometer, Thermo Scientific Xcalibur software. [c]$[M_{mono} + (z \times 1.00728)]/z$. [d]$(M_{meas} - M_{mono(calc)})/M_{mono(calc)} \times 10^6$. [e]Exformma EX1600 analytical HPLC system with a YMC-Pack ODS-A C_{18} (100 Å, 4.6 × 150 mm) column. Gradient: 0−5 min 0% B, 5−15 min 0−60% B, and 15−25 min 60−100% B; flow rate: 1 mL/min; detector wavelength: λ = 220 nm. Eluent A: 0.1% (v/v) TFA in water and eluent B: 0.1% (v/v) TFA in acetonitrile:water = 80:20 (v/v). [f]Published in ref 64.

A

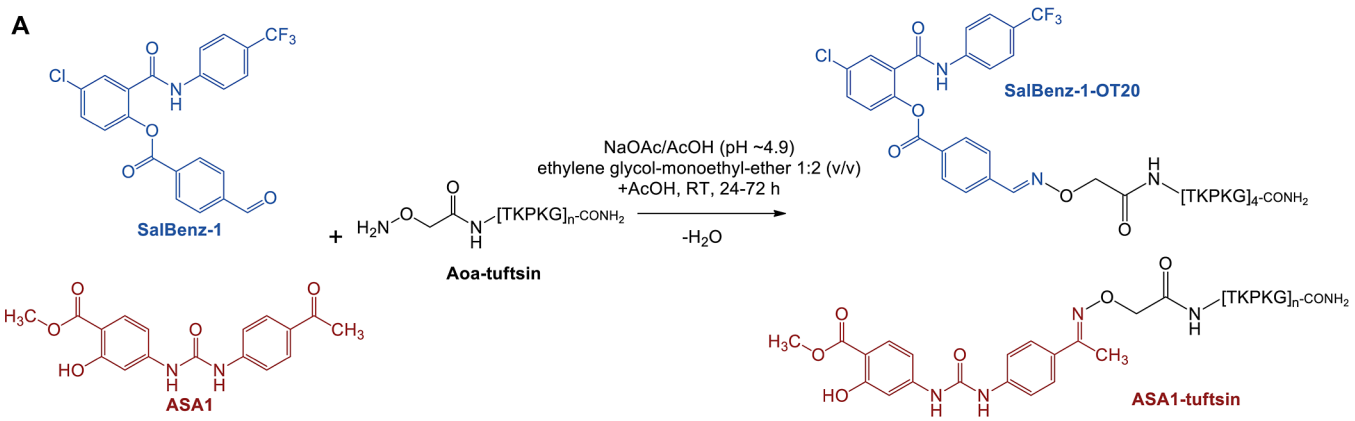

B

Code	$Mw_{av(calc)}$[1]	$Mw_{mono(calc)}$[1]	Measured m/z[2]	Calculated m/z[3]	ppm[4]	R_t (min)[5]
SalBenz-1-OT20	2566.3168	2564.3282	428.3942	428.3953	-2.6	14.7
ASA1-OT5*	912.0002	911.4501	912.4578	912.4574	0.5	15.4
ASA1-OT10*	1423.6152	1422.7619	1247.7108	1247.7107	0.1	14.8
ASA1-OT15	1935.2301	1934.0738	484.5252	484.5257	-1.1	13.2
ASA1-OT20	2446.8451	2445.3856	408.5705	408.5716	-2.8	13.6

Figure 2. Synthesis and characterization of the salicylanilide−tuftsin conjugates. (A) Formation of the oxime bond between the salicylanilide derivatives and the carrier peptides. (B) Characterization of the conjugates. [1]Average and monoisotopic masses were calculated using CS ChemOffice Pro ver. 12.0. [2]Q Exactive Focus Hybrid Quadrupole-Orbitrap Mass Spectrometer; Thermo Scientific Xcalibur software.[3]$[M_{mono} + (z \times 1.00728)]/z$.[4]$(M_{meas} - M_{mono(calc)})/M_{mono(calc)} \times 10^6$.[5]Exformma EX1600 analytical HPLC system with YMC-Pack ODS-A C_{18} (100 Å, 4.6 × 150 mm) column. Gradient: 0−5 min 0% B, 5−15 min 0−60% B, and 15−25 min 60−100% B; flow rate: 1 mL/min; detector wavelength: λ = 220 nm. Eluent A: 0.1% (v/v) TFA in water; eluent B: 0.1% (v/v) TFA in acetonitrile:water = 80:20 (v/v). *Data also presented in ref 64.

with NucBlue (Hoechst 33342) counterstain (Thermo Scientific) and performed imaging subsequently.

On day six, we changed the medium on the TW monolayers before the Cf-peptide treatment. The solution of the Cf-peptide was applied on the apical side (12.5, 25, and 50 μM concentrations for 90 min, 37 °C, 5% CO_2). We removed the TWs after incubation. As detector cells, U87 cells were employed on the basolateral side. The U87 cells' Cf-peptide uptake was investigated by flow cytometry (BD LSR II). As controls, U87 cells were treated in the absence of TW inserts, and to this end, we seeded U87 cells (10^5 cells/well in CM DMEM) on 24-well plates on day four before treatment.

In Vitro Penetration of Cf-Peptides on Agarose Dish-Based U87 Spheroids. For the spheroid formation and treatment, we used a modified method based on earlier works.[60,64] Briefly, we filled the polydimethylsiloxane (PDMS) micromolds used for casting 3D petri dishes (MicroTissues, 5 × 7 array, Sigma) with molten agarose solution (2%, w/v in PBS). After gelation, we equilibrated the agarose dishes with DMEM ICM (2 mL medium, 2 h, 37 °C). We seeded the cells in 14 μL of cell suspension (7.1×10^3 cell /μL in DMEM CM). Before seeding the cells, we stained cell nuclei with Hoechst 33342 (1 μM in DMEM ICM) for 30 min.[60,64] We incubated the stained and seeded cells in 2 mL of DMEM CM for 48 h, while spheroids formed due to cell-to-cell adhesion and aggregation. We monitored the aggregation process by capturing phase-contrast images with a Zeiss Axio Observer Z1 microscope equipped with a 10× Plan-Neofluar objective and a Marzhauser motorized stage. The microscope was controlled by Zeiss Axiovision 4.8 software, enabling it to capture large mosaic images of 6 × 11 fields of view, covering the entire area of the spheroids in the microwells.

After the incubation for 48 h, we washed the spheroids twice with ICM DMEM and treated the spheroids in the microwells

https://doi.org/10.1021/acsomega.3c05727
ACS Omega 2024, 9, 16927−16948

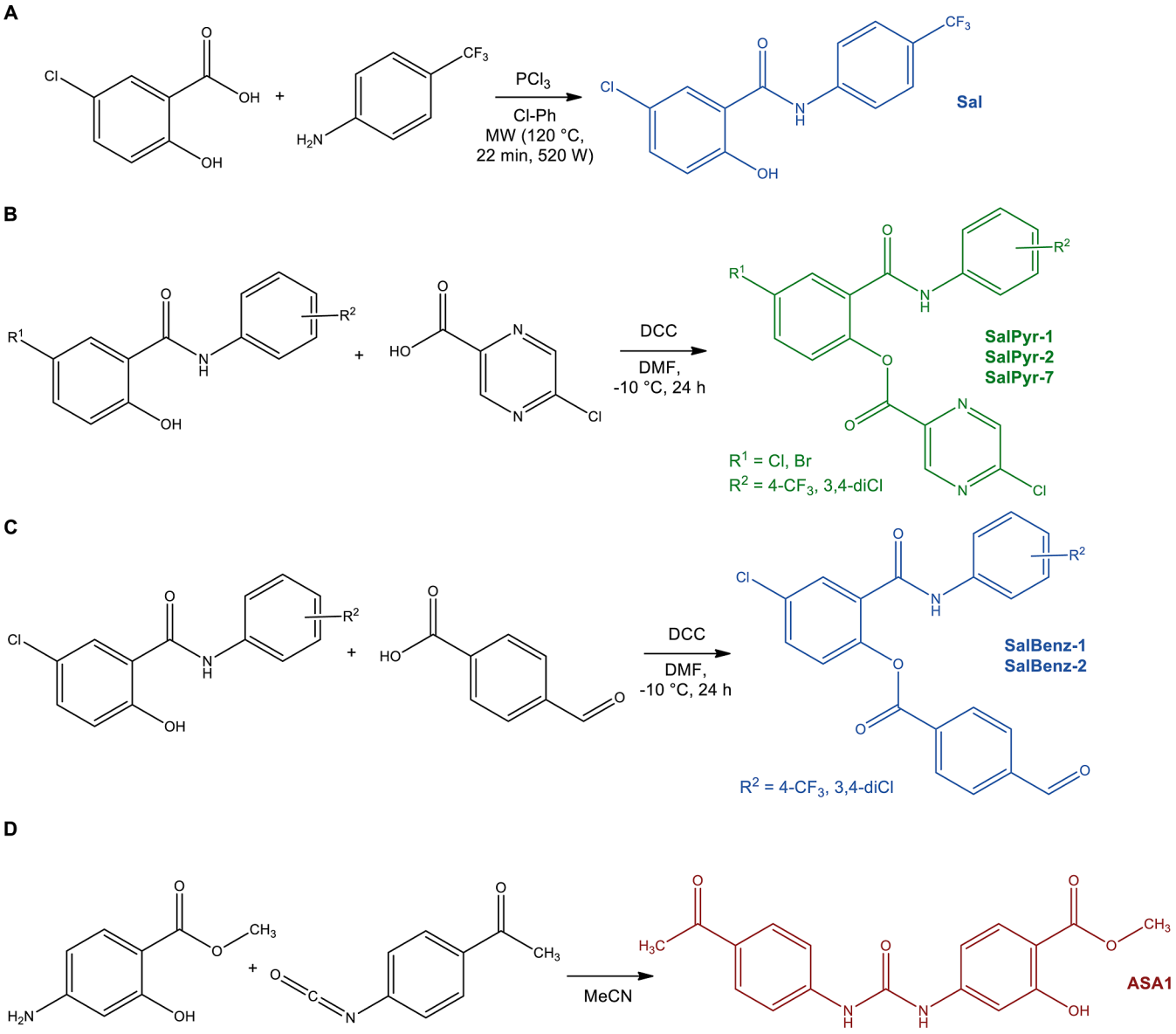

Figure 3. Synthesis of the salicylanilide derivatives (A) Sal.[61,62] (B) Salicylanilide 4-formylbenzoates (SalBenz-1 and SalBenz-2). (C) 5-Chloropyrazine-2-carboxylic acid derivatives (SalPyr-1, SalPyr-2, and SalPyr-7)[62] and (D) ASA1.[64] Ph−Cl: chlorobenzene; DMF: *N*,*N*-dimethylformamide; DCC: *N*,*N*′-dicyclohexylcarbodiimide; MeCN: acetonitrile.

with the Cf-OT15 and Cf-OT20 peptides (25 μM/2 mL of ICM DMEM for 1.5 h). Following the treatment, we washed the spheroids two times with ICM DMEM and then three times with PBS. We used a Zeiss Axio Observer Z1 inverted epifluorescent microscope (10× Plan Neofluar or 40× EC Plan-Neofluar objectives) for capturing phase-contrast and fluorescent images. Focusing and stage positioning for multifield mosaic imaging were controlled by Zeiss Axiovision 4.8 software. We processed the mosaic images using NIH ImageJ software.

After imaging and harvesting a representative set of spheroids for trypsinization, the remaining spheroids were fixed in the agarose dishes with 4% PFA for 15 min (37 °C). Flow cytometry analysis of the harvested live (nonfixated) spheroids (6−6 spheroids from each treatment) was carried out after 16 min of trypsinization. Trypsin activity was stopped by adding HPMI supplemented with 10% FBS. Subsequently, we transferred the cells into FACS tubes (Sarstedt), centrifuged the suspension (1000 rpm, 5 min), and, finally, added HPMI to the cells after removing the supernatant. The flow cytometry measurement (gating and analysis) was similar to that described in the section "*In Vitro* Internalization Studies".

RESULTS AND DISCUSSION

The substituted salicylanilide derivative Sal has a remarkable antitumor effect on U87 GBM cells.[60] In our previous studies, the 4-aminosalicylic acid derivative ASA1 had a cytostatic effect on HepG2 hepatocellular carcinoma cells,[64] and salicylanilide 5-chloropyrazinoates (SalPyr-1, SalPyr-2, and SalPyr-7) had significant cytostatic activity on MonoMac6 human monocyte cell culture.[62] In addition to these compounds, two new esters, the salicylanilide 4-formylbenzoates (SalBenz-1 and SalBenz-2), were synthesized and investigated. Moreover, to evaluate the effect of conjugation,

https://doi.org/10.1021/acsomega.3c05727
ACS Omega 2024, 9, 16927−16948

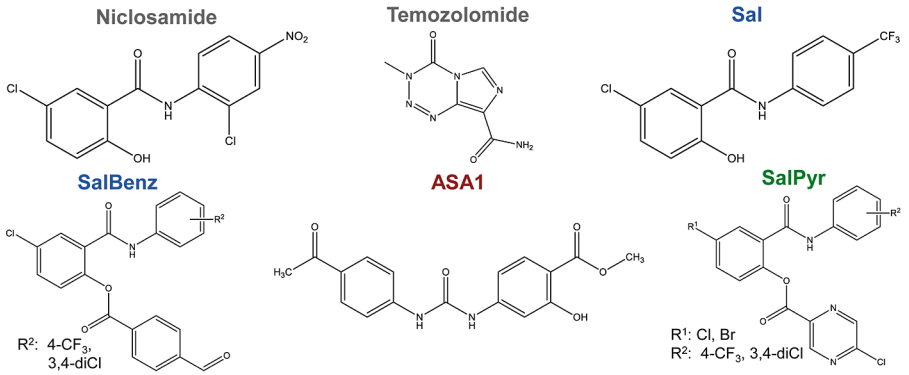

Compound/ Formula	LogP[a]	Solubility category/ Intrinsic solubility[b]	Mw	Hydrogen bond donor/acceptor[c]	Molar refractivity[d] (cm^3/mol)	Lipinski rule
Niclosamide	3.910	Low/-3.475	325.99	2/4	79.5	✓
Temozolomide	-0.283	High/-0.896	194.10	1/5	47.86	✓
Sal	4.243	Low/-4.922	315.03	2/2	74.35	✓
SalBenz-1	5.921	Low/-7.226	447.05	1/3	110.76	×
SalBenz-1-OT20	-10.512	no data	2564.33	30/37	648.04	×
SalBenz-2	6.251	Low/-7.639	446.98	1/3	114.39	×
ASA1	3.026	High/-3.636	328.32	3/4	90.46	✓
ASA1-OT5	-2.881	High/-3.599	912.01	11/14	236.94	×
ASA1-OT10	-7.07	High/0.487	1423.64	18/22	367.21	×
ASA1-OT15	-10.818	no data	1934.07	25/30	497.48	×
ASA1-OT20	-13.407	no data	2445.39	32/38	627.75	×
SalPyr-1	4.783	Low/-6.601	455.01	1/4	105.35	✓
SalPyr-7	5.113	Low/-7.014	454.94	1/4	108.99	×
SalPyr-2	5.278	Low/-7.189	498.89	1/4	111.81	×

Figure 4. Chemical characterization of the compounds. [a]log *P*,[b]intrinsic solubility,[c]the number of hydrogen bond donors and acceptors, and[d]molar refractivity were predicted by www.chemicalize.com/ChemAxon.[129,130] Niclosamide [$C_{13}H_8Cl_2N_2O_4$, 5-chloro-*N*-(2-chloro-4-nitrophenyl)-2-hydroxybenzamide], TMZ [$C_6H_6N_6O_2$, 3-methyl-4-oxo-3*H*,4*H*-imidazo(4,3-*d*)(1,2,3,5)tetrazine-8-carboxamide], Sal {$C_{14}H_9ClF_3NO_2$, 5-chloro-2-hydroxy-*N*-[4-(trifluoromethyl)phenyl]benzamide}, SalBenz-1 ($C_{22}H_{13}ClF_3NO_4$, 4-chloro-2-{[4-(trifluoromethyl)phenyl]carbamoyl}phenyl 4-formylbenzoate), SalBenz-2 {$C_{21}H_{12}Cl_3NO_4$, 4-chloro-2-[(3,4-dichlorophenyl)carbamoyl]phenyl 4-formylbenzoate}, ASA1 ($C_{17}H_{16}N_2O_5$, methyl 4-{[(4-acetylphenyl)carbamoyl]amino}-2-hydroxybenzoate), SalPyr-1 ($C_{19}H_{10}Cl_2F_3N_3O_3$, 4-chloro-2-{[4-(trifluoromethyl)phenyl]carbamoyl}-phenyl 5-chloropyrazine-2-carboxylate), SalPyr-7 {$C_{18}H_9Cl_4N_3O_3$, 4-chloro-2-[(3,4-dichlorophenyl)carbamoyl]phenyl 5-chloropyrazine-2-carboxylate}, and SalPyr-2 {$C_{18}H_9BrCl_3N_3O_3$, 4-bromo-2-[(3,4-dichlorophenyl)carbamoyl]phenyl 5-chloropyrazine-2-carboxylate}.

peptide conjugates (ASA1-OT5, ASA1-OT10, ASA1-OT15, ASA1-OT20, and SalBenz-1-OT20) were examined.

Synthesis and Characterization of Carrier Peptides and Conjugates. Carrier peptides were synthesized by a manual method using the Fmoc/^{t}Bu strategy. For the synthesis, Fmoc-Rink Amide MBHA resin was used. Acetylated (Ac-) and 5(6)-carboxyfluorescein (Cf-) peptides were synthesized. The homogeneity of the peptides was determined with the help of analytical HPLC using a reverse-phase column. Mass accuracy was verified using high-resolution mass spectrometry (Table 2). Homogeneity and appropriate mass accuracy were confirmed. Analytical chromatograms along with the mass spectra are shown in Supporting Information Figures S1−3. The fluorescence properties of Cf-peptides were also determined, as presented in Supporting Information Figures S4−5. All Cf-tuftsin derivatives have pH-dependent fluorescence intensity.

For conjugation, the *N*-terminal of the peptide was (aminooxy)acetylated (Aoa-). An oxime bond was formed between the Aoa-peptides and the carbonyl group of SalBenz-1 and ASA1 (Figure 2A) under slightly acidic conditions in the liquid phase. Reactions were monitored using an analytical RP-HPLC system for 24 h. Chromatograms are shown in the Supporting Information (Supporting Information Figures S6−8). Reaction mixtures were purified with a semipreparative RP-HPLC system, and products were analyzed with analytical RP-HPLC and high-resolution mass spectrometry (Figure 2B). All products were homogeneous with appropriate mass accuracy. Analytical chromatograms and mass spectra are shown in Supporting Information Figures S9−11.

Synthesis and Stability of the Salicylanilide Derivatives. Sal was prepared as previously described,[61,62] by the reaction between 5-chloro-2-hydroxybenzoic acid and 4-(trifluoromethyl)aniline with the addition of phosphorus trichloride (0.5 equiv) in chlorobenzene (Figure 3A). The reaction was carried out in a microwave reactor for 22 min to reflux. This procedure increased yield and shortened reaction time from several hours to minutes.[119] The details of the synthesis and chemical and structural characterization are presented in Supporting Information page S16.

The new esters, salicylanilide 4-formylbenzoates (SalBenz-1 and SalBenz-2), were obtained by the esterification of substituted salicylanilides with 4-formylbenzoic acid, activated by *N*,*N*′-dicyclohexylcarbodiimide (DCC) in DMF (Figure 3C). High-resolution mass spectra of the compounds can be seen in Supporting Information Figures S12−13.

4-Aminosalicylic acid derivative (ASA1) was prepared with the reaction of methyl 4-aminosalicylate and 4-acetylphenyl isocyanate in acetonitrile (Figure 3D), as described in ref 64.

https://doi.org/10.1021/acsomega.3c05727
ACS Omega 2024, 9, 16927−16948

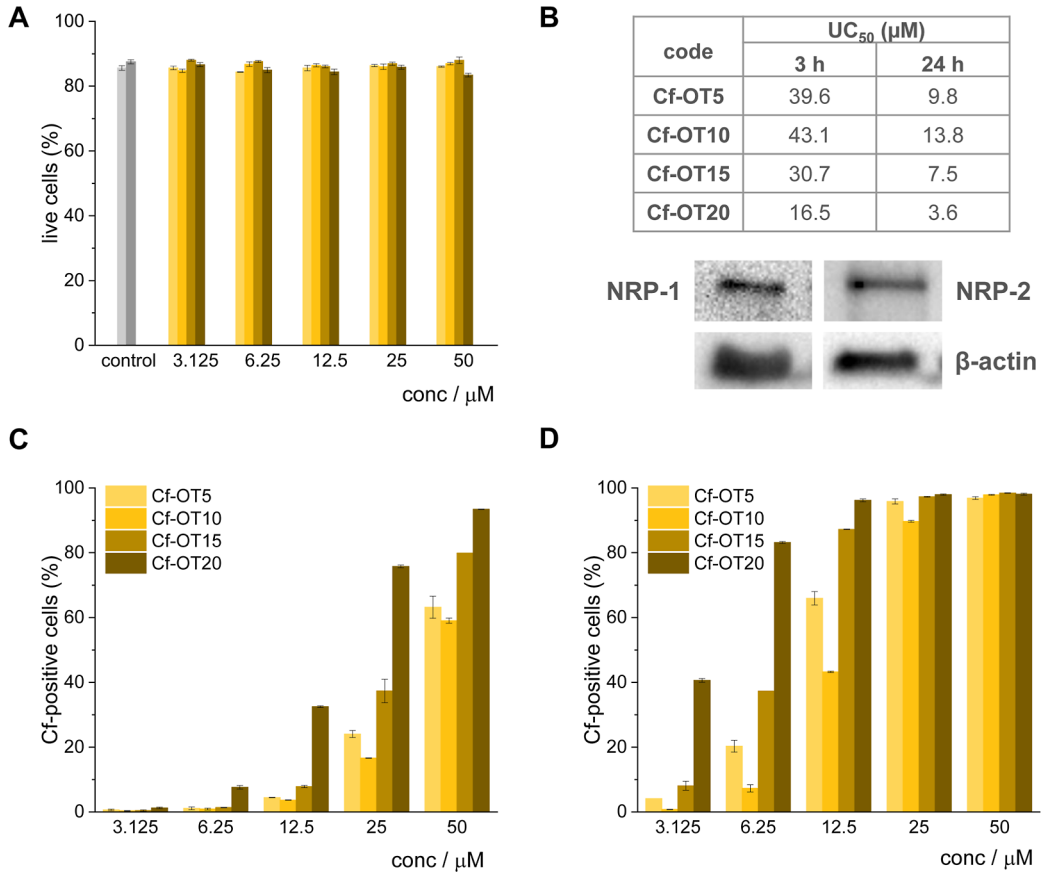

Figure 5. *In vitro* internalization of the Cf-peptides on U87 cells. Treatment conditions: 3.125−50 μM concentration range, 3 h, 24 h. (A) Relative viability of the cells compared to the untreated (light gray) and DMSO (dark gray) controls. (B) Calculated UC_{50} values and the NRP content of U87 cells were detected from whole cell lysates by Western blot analysis. Ratio of Cf-positive live cells after (C) 3 h and (D) 24 h of treatment.

For the chemical and structural characterization, see Supporting Information page S16.

Salicylanilide 5-chloropyrazinoates (SalPyr-1, SalPyr-2, and SalPyr-7) were prepared by the esterification of substituted salicylanilides with 5-chloropyrazine-2-carboxylic acid by the previously described activation by DCC (Figure 3B).[62] For details, see Supporting Information page S16−17.

The stability of the parent salicylanilide Sal and the selected compounds SalBenz-1, ASA1, and SalPyr-1 were investigated in DMSO and culture medium (serum-free RPMI-1640 containing 10% DMSO) at 37 °C, sampling over at least 48 h and modeling the *in vitro* conditions. Analytical RP-HPLC and ESI-MS were used. No decomposition was observed in the case of Sal, SalBenz-1, and ASA1, nor in DMSO (Supporting Information Figures S14−17), nor in the culture medium (Supporting Information Figures S18−19), even after 90 h. The salicylanilide-5-chloropyrazinoate SalPyr-1 was decomposed in a culture medium after 40 h of incubation (Supporting Information Figure S20). The parent salicylanilide Sal, as determined by ESI-MS, was coeluted with its ester, the appearance of 5-chloropyrazine-2-carboxylic acid, was indicative of decomposition. The half-time of SalPyr-1 was calculated by the percentage of the released 5-chloropyrazine-2-carboxylic acid (Supporting Information Figure S21). The half-time of SalPyr-1 was estimated to be above 5 h.

Characterization of Compounds Using the Chemicalize Online Platform. Chemicalize was used to determine the compound characteristics important for drug-likeliness such as the log *P* value, intrinsic solubility, molecular weight, and number of hydrogen bond donors/acceptors. Based on these data, it was possible to determine whether the compounds fulfill the criteria of Lipinski's rule of five. Figure 4 presents the calculated data and the IUPAC name of the compounds.

The substituted salicylanilide Sal, the 4-aminosalicylic acid derivative ASA1, and one of the salicylanilide 5-chloropyrazinoates (SalPyr-1) meet the Lipinski rule. The other derivatives (salicylanilide 4-formylbenzoates: SalBenz-1, SalBenz-2, and the salicylanilide 5-chloropyrazinoates SalPyr-7 and SalPyr-2) have a higher log *P* than 5.0; thus, these compounds fail the Lipinski rule. The solubility of the salicylanilide derivatives in the aqueous phase is increased after conjugation to tuftsin derivatives. The number of tuftsin units has an effect: the longer the peptide, the lower the log *P* values.

***In Vitro* Internalization and Intracellular Localization of the Cf-Peptides.** The *in vitro* internalization of the Cf-tuftsin derivatives was measured based on the intracellular fluorescence using flow cytometry. Before the measurements, the fluorescence properties of the Cf-peptides were determined, as shown in the Supporting section (SF4−5). For the internalization studies, U87 cells were treated with the peptides for 3 or 24 h in the concentration range of 3.125−50 μM. During the analysis, the *in vitro* cytotoxic effect of the Cf-peptides was also determined. The percentage of living cells was at least 80% in all cases, and no cytotoxic effect of the Cf-tuftsins was observed even after 24 h of treatment at 50 μM (Figure 5A). UC_{50} values—the interpolated concentration at

https://doi.org/10.1021/acsomega.3c05727
ACS Omega 2024, 9, 16927−16948

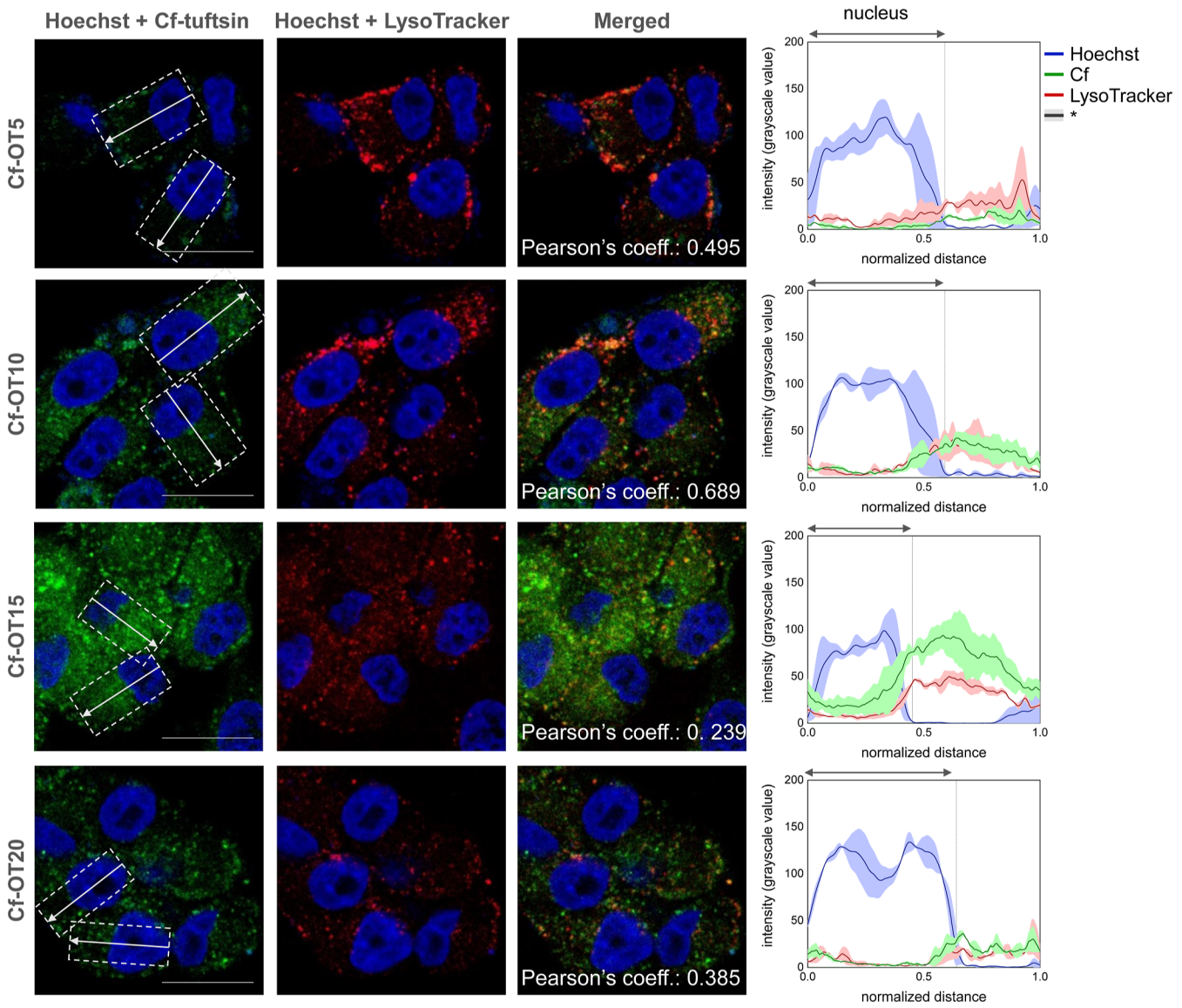

Figure 6. *In vitro* intracellular localization of Cf-tuftsin peptides. Confocal microscopy images of U87 cells treated with Cf-tuftsins (3 h, 25 μM). Blue: nucleus (Hoechst 33342), green: Cf-tuftsins (5(6)-carboxyfluorescein), and red: lysosomes (LysoTracker Deep Red). For imaging, the Zeiss LSM 710 system was used; the scale bar represents 20 μm. Line scan analysis was performed by NIH ImageJ software using the Plot Profile application. *Standard error was calculated and visualized by OriginPro 2018 software.

which 50% of the cells show intracellular fluorescence[117]—are summarized in Figure 5B. As tuftsin-like sequences are ligands of neuropilins, the NRPs were detected with the Western blot method from whole cell lysates. Both NRP-1 and NRP-2 are present in the cell lysates (Figure 5B). These receptors can serve as an entry route for the oligotuftsin derivatives by receptor-mediated endocytosis.

The internalization of the peptides is time- and concentration-dependent (Figure 5C,D). The number of tuftsin units ($[TKPKG]_n$, n = 1−4) also has an effect; the internalization is highest in the case of Cf-OT20 (n = 4), followed by Cf-OT15 (n = 3), Cf-OT5 (n = 1), and Cf-OT10 (n = 2). Cf-OT20 (UC_{50} = 16.5, 3.6 μM) has remarkably higher internalization compared to the other tuftsin derivatives (UC_{50} > 30.7, 7.5 μM). In all cases, the internalization after 3 h of treatment (Figure 5C) was lower than that after 24 h of treatment (Figure 5D) based on the ratio of Cf-positive live cells. The mean fluorescence intensity (MFI) values also confirm these tendencies, as shown in the Supporting Information (Figure S22).

Intracellular localization of Cf-peptides was determined by using confocal laser scanning microscopy. U87 cells were treated with Cf-peptides (25 μM) for 3 h. Before this analysis, a preliminary experiment was carried out to compare the intracellular localization on live and fixed cells (see Supporting Information, Figure S24 and description). Based on those and our previous results[60,64,131] for confocal microscopy, we have used fixed cells. The internalization pathway was studied by staining lysosomes with LysoTracker Deep Red. Representative images are presented in Figure 6. All tuftsin derivatives have partial colocalization with the lysosomal staining, and diffuse cytosolic localization can also be observed. This indicates a mixed internalization route, with possible direct translocation and receptor-mediated endocytosis via the NRP receptors. To quantify the visible differences in the localization of the Cf-tuftsins, we carried out grayscale analysis of the

https://doi.org/10.1021/acsomega.3c05727
ACS Omega 2024, 9, 16927−16948

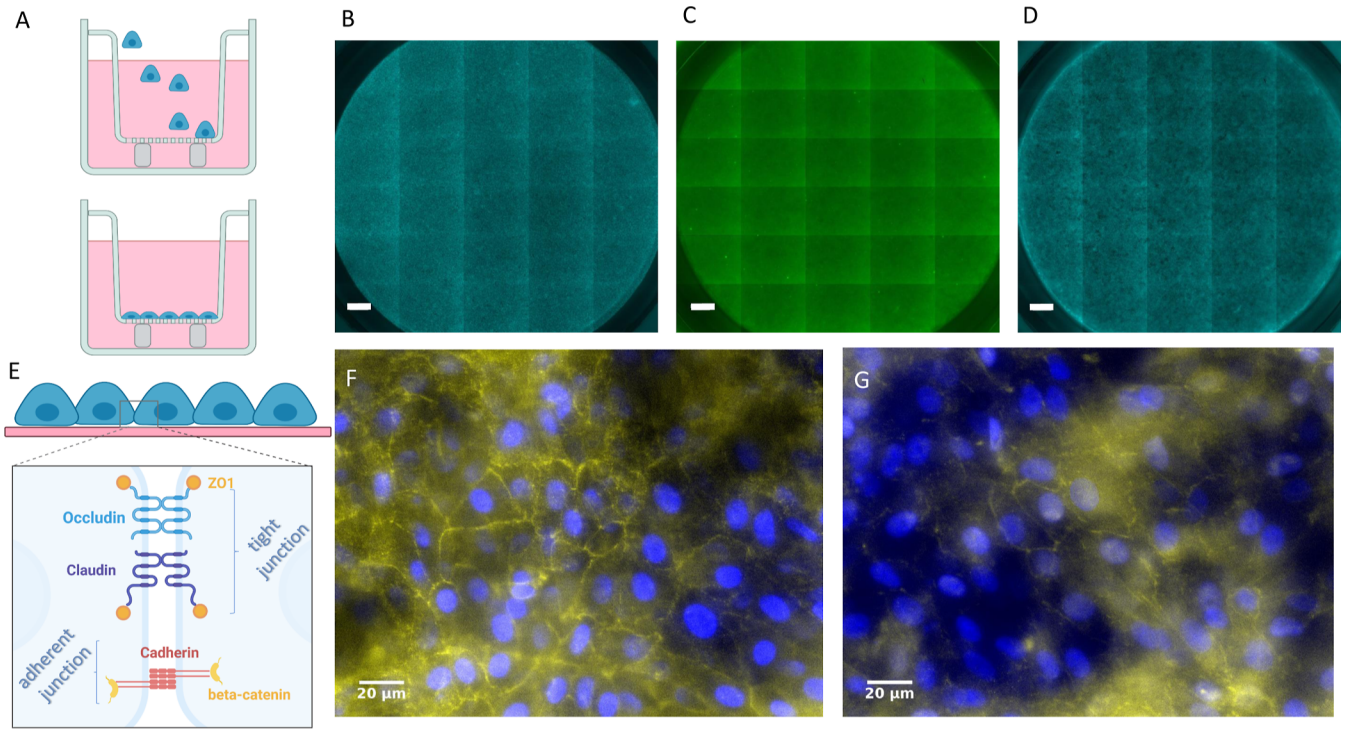

Figure 7. Characterization of the integrity of the HUVEC monolayer on the apical side of the TW insert. (A) Schematic representation of the microporous polycarbonate membrane and cell seeding (day 1) and HUVEC monolayer (day 5). (B–D) The enlarged features of the monolayer were imaged *in situ* for mosaic multifield image acquisition, nuclei were stained with Hoechst (blue; before treatment B; after treatment D, Day 5), and cells were treated with peptide Cf-OT20 on day 5 (50 mM, 1.5 h, C). The scale bar represents 500 μm (B–D). (E) Schematic representation of tight and adherent junctions with ZO1 and β-catenin markers. (F,G) Representative enlarged sections with β-catenin (yellow, F) and ZO1 (yellow, G) immunolabeling on a mounted excised membrane stained with Hoechst (blue). The scale bar represents 20 μm (F,G).

images. We carefully optimized the treatment and the staining and fixation process of the U87 cells to assess comparable grayscale values corresponding to green (intensity of Cf) and red (intensity of LysoTracker dye) signals. Laser intensity values were identical in the case of all Cf-tuftsin peptides. For image processing, ZEN 3.0 blue lite software was used, and grayscale values were extracted using NIH ImageJ software's Plot Profile application.

Cf-OT5, Cf-OT10, and Cf-OT20 showed accumulation mainly in lysosomal compartments (based on lysosomal staining) (Figure 6). Colocalization with the lysosomal staining may indicate endocytosis and vesicular transport as a mechanism for the uptake of Cf-peptides. In the case of these peptides, the green and the red signals are of roughly similar intensity, and this similarity is most expressed on the areas where the signal (grayscale value) is high. The Cf signal only partially colocalizes with the cytoplasmic area. No colocalization with the nuclei staining can be observed, as proved also by the line scan analysis of the representative cells (presented with low Hoechts intensity).

According to the fluorescent signals, Cf-OT15 is mainly localized in the cytoplasm, while is also accumulated in the cytosol and partially colocalized with the lysosomal staining and shows a different pattern. If the Cf-peptide internalizes into the lysosome, then the green and red signals colocalize (exhibit similar intensity in the function of the normalized distance); when the Cf-peptide is in the cytoplasm, then the graphs of the signals show different intensity.

We have also evaluated the colocalization using ImageJ JACoP.[132,133] The calculated values presented similar tendencies to what was obtained from the grayscale analysis. The Pearson's coefficient value for Cf-OT5, Cf-OT10, and Cf-OT20 (0.495, 0.689, and 0.3852, respectively, regarding the green and red channel) suggests correlation with mixed localization. In the case of Cf-OT15, the coefficient value (0.239) suggests small correlation and, therefore, mainly cytoplasmic occupation. Each approach (grayscale analysis and JaCop) has its limitation and we have mainly designed our experiments for qualitative rather than quantitative comparisons.

***In Vitro* Penetration of Cf-Tuftsin Peptides on a Simple HUVEC-U87 Blood–Brain Barrier Model.** TW inserts as permeable supports feature a microporous membrane, and on these membranes, monolayers can be cultured to mimic tissue barriers with modeling conditions that occur in the *in vivo* environments. In our study, noncontact, submerged coculture monolayers were used as a simple *in vitro* blood–brain barrier model, based on our previous results[60] (Figure 7). On the membrane of the apical chambers, HUVEC cells were seeded, and on the basolateral surfaces, U87 monolayers were applied as detector cells. To determine the penetration ability of the Cf-peptides, quantitative flow cytometry analysis was used. After the treatments with the Cf-peptides, the ratio of live and Cf-positive cells and intracellular fluorescence intensities of the detector cells were analyzed.

Before the Cf-peptide treatments, it is necessary to determine the confluency of the HUVEC monolayers on the apical membrane (Figure 7A). For this, *in situ* imaging with Hoechst staining, zonula ocludens-1 protein (ZO1), and β-catenin immunolabeling were performed. Based on the nuclei staining (before the transport experiment), a confluent

https://doi.org/10.1021/acsomega.3c05727
ACS Omega 2024, 9, 16927–16948

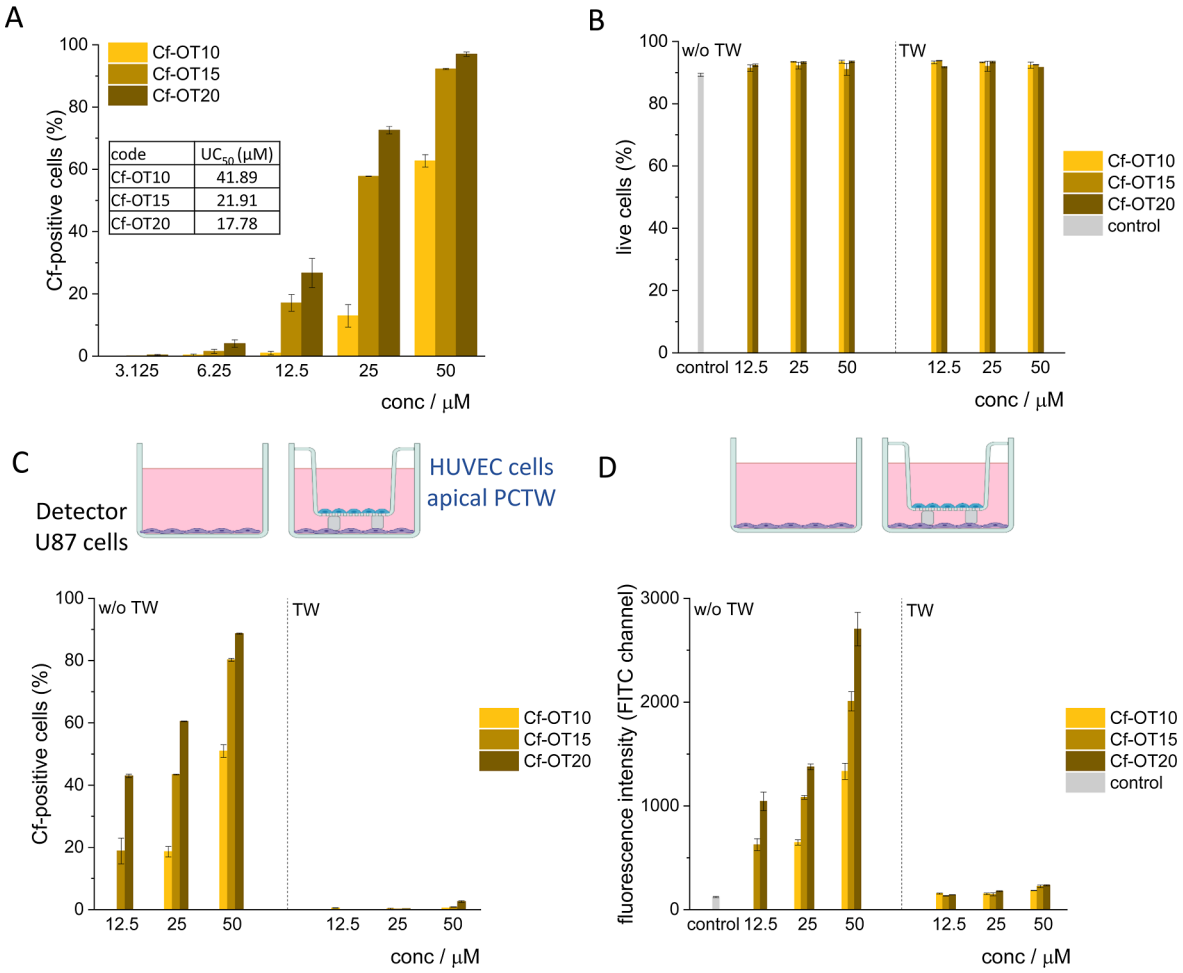

Figure 8. Penetration ability of Cf-peptides was quantified by flow cytometry using TW inserts mimicking the blood−brain barrier. (A) The uptake rate of HUVEC cells and (B) the viability of the detector U87 cells were monitored by flow cytometry following the treatment with Cf-peptides (12.5−50 μM concentration range, 90 min incubation time). (C, D) Schematic representation of the TW experiment setup and the coculture arrangement of noncontact submerged monolayers containing HUVEC cells with a detector U87 cells. HUVEC were seeded into the apical chamber of the TW insert (on polycarbonate membrane, PCTW), while U87 cells were seeded into the basolateral chamber (with or w/o TW insert). Cellular uptake of peptides Cf-OT10, Cf-OT15 and Cf-OT20 in U87 detector cells with or w/o TW inserts was compared with regard to the percentage of Cf-positive cells and MFI values.

monolayer was formed (Figure 7B). After the treatment with Cf-peptides, the membranes were imaged to visualize the internalized peptides (Figure 7C,D; see also: Figure S25). β-Catenin is a marker of adherent junctions; ZO1 is one for tight junctions (Figure 7E). The immunolabeling was carried out on the fixed, excised, and mounted membrane; adherent and tight junctions were detected between HUVEC cells (Figure 7F,G).

Initially, the penetration ability of the Cf-tuftsins was studied on HUVEC model cells. Moderate cellular uptake was measured in HUVEC cells. We determined the UC_{50} values on HUVEC cultures regarding Cf-OT10, Cf-OT15, and Cf-OT20 (Figures 8A and S26). The Cf-peptides were uptaken after 90 min of treatment. After these measurements, we worked on the TW systems. After the formation of confluent monolayers (usually 5−6 days after seeding), the apical chambers were treated with Cf-tuftsin peptides, at 12.5, 25, or 50 μM concentration for 90 min. Treatments without TWs were also carried out as control experiments to determine the internalization (Figure 8).

Flow cytometry was applied to determine the cellular uptake rate of the Cf-tuftsin derivatives by U87 cells that followed the penetration through the HUVEC apical monolayer. Our data showed that the viability of the U87 cells was not affected by the TW inserts and after the Cf-peptides' treatment (Figures 8B and S25−26). The cellular uptake of Cf-peptides in the detector cell layer was higher without TW inserts, as expected (Figure 8C,D). Based on the percentage of Cf-positive cells and mean fluorescence intensities, the penetration through the HUVEC layer is Cf-peptide- and concentration-dependent. A low uptake rate was observed with TW inserts after 90 min of treatment at 50 μM concentration in the case of Cf-OT20 (see also Figure S26−27). For Cf-OT10 and Cf-OT15, no significant fluorescent signal was detected compared to untreated controls. We have determined that Cf-tuftsins up to 50 mM concentration could penetrate HUVEC cellular layers while retaining the cells' full viability and functionality. In our studies, the Cf-peptides did not cause any change in monolayer integrity.

***In Vitro* Penetration of Cf-Peptides on Agarose Dish-Based U87 Spheroids.** The penetration ability of Cf-peptides was assessed on spheroids created from U87 cells employed as a simple tumor model.

We successfully used agarose-based spheroids, as demonstrated before.[60,64,131] Before the spheroid preparation, the

https://doi.org/10.1021/acsomega.3c05727
ACS Omega 2024, 9, 16927−16948

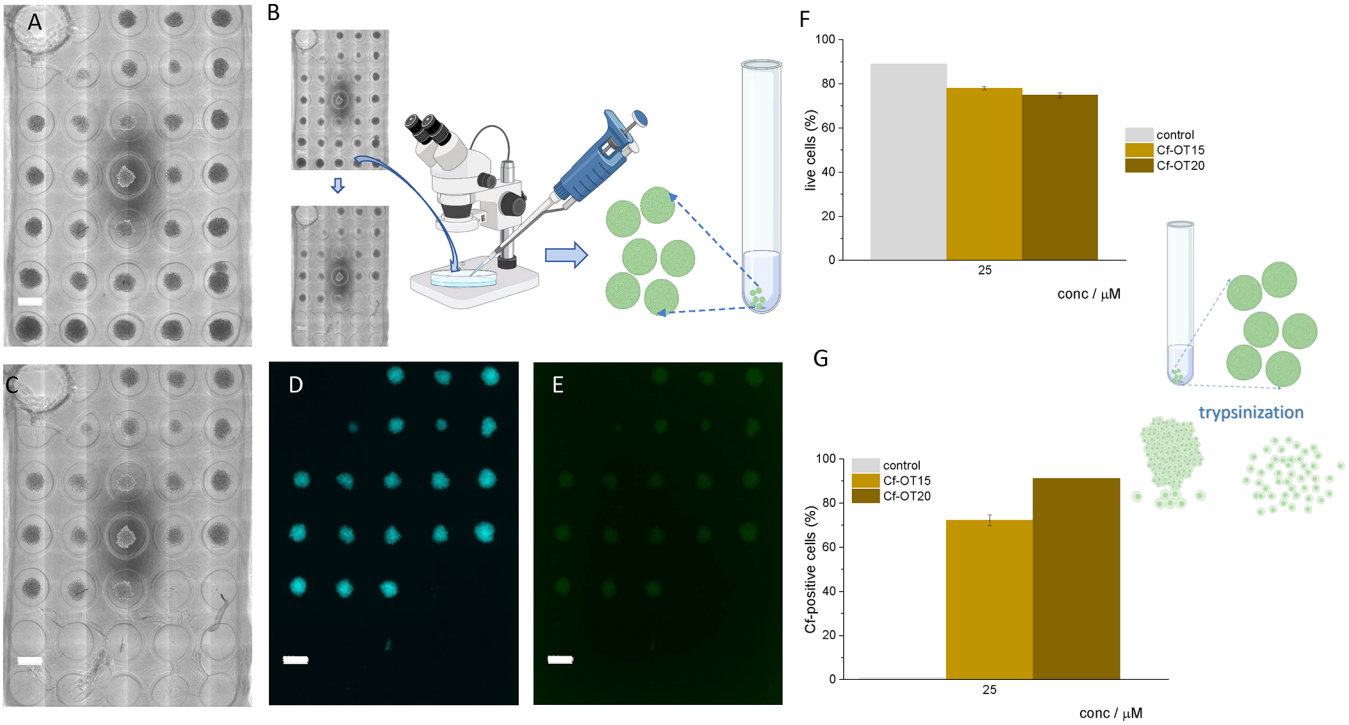

Figure 9. Employing agarose dish-based U87 spheroids to assess penetration ability of Cf-peptides. (A) Phase-contrast mosaic image of U87 cells seeded in a 35-microwell agarose dish for aggregation (day 1). (B) U87 spheroid formation on day 2 (upper image) and day 3 (lower image) and schematic representation of the spheroid's harvesting for flow cytometry analysis after Cf-peptide treatment. (C) Phase-contrast imaging of the spheroids on day 3; after Cf-OT20 treatment and before fixation, several spheroids were removed from lower rows of the dish for flow cytometry analysis. (D) Fluorescent imaging of the same dish as in (C) and visualization by Hoechst staining (blue). (E) Fluorescent visualization of the Cf-peptide (green) in the same dish as in (C,D). Scale bar in A–E: 500 μm. (F,G) Flow cytometry results of live (nonfixed) U87 spheroids after 16 min of the trypsinization process. (F) Relative ratio of live cells compared to control live, trypsinized, and untreated spheroids; (G) Cf-positive cells after trypsin treatment resulting in single cell suspension.

nuclei were labeled with Hoechst. The cellular uptake and cell viability were also checked on Hoechst-labeled and nonlabeled cells; the internalization rates and the viability were not affected (Figure S28). In this study, the aggregation process was monitored within these agarose blocks by phase-contrast and fluorescent microscopy, as demonstrated in Figure 9 (Figures S29–30). The agarose dish preparation was a labor-intensive procedure, but these blocks were stable through the treatment, imaging, and fixation steps. The produced U87 spheroids possessed an average diameter of 400–450 μm (Figure 9; see also: Figures S29–30). Spheroids were treated with 25 μM Cf-OT15 and Cf-OT20 for 1.5 h. The treated spheroids were harvested and trypsinized to break up the spheroids to get single-cell suspension and then analyzed with flow cytometry. Digestion with trypsin results in killing a small percentage of the cells; however, this measurement was suitable to differentiate the penetration ability between Cf-OT15 and Cf-OT20 peptides. Altogether, peptides Cf-OT15 and Cf-OT20 had fair penetration ability on U87 spheroids. Peptide Cf-OT20 had a slightly higher number of Cf-positive cells, but the difference was not significant.

Compounds' Effect on Autophagy on U87 Glioma Cell Culture. Autophagy is a catabolic process which is generally activated by nutrient deprivation, differentiation, neurodegenerative diseases, infection, and cancer. Autophagy can induce programmed cell death processes such as apoptosis or autophagy-dependent cell death.[32] Autophagy marker LC3 is a subunit of microtubule-associated proteins 1A and 1B (termed MAP1LC3). LC3 is a soluble protein which is present in mammalian tissues and also cultured cells. A cytosolic form of LC3 (LC3-I) is conjugated to phosphatidylethanolamine (PE) to form the LC3-PE conjugate (LC3-II), which is recruited to autophagosomal membranes. Immunoblotting is a reliable method for monitoring autophagy and detecting LC3 and autophagic cell death; since LC3 is the only protein identified on the inner and outer membranes of autophagosomes. Autophagy can be determined by changes in LC3 localization, and the level of conversion of LC3-I to LC3-II provided us with an indicator of activity. It is important to note that the levels of LC3-II correlate with autophagosome formation due to its association with the autophagosome membrane. The LC3 was detected as two bands; cytosolic LC3-I and LC3-II, which are bound to PE in the autophagosome membrane. This makes the molecular weight of LC3-II higher than that of LC3-I. However, due to its hydrophobicity, LC3-II migrates faster in SDS-PAGE and therefore displays a lower apparent molecular weight.[25,134]

Autophagy triggering was studied on human U87 GBM cells using Western blot analysis (Figure 10A,B). To enumerate the autophagy-inducing effect of the compounds, densitometry analysis was performed. The ratio of LC3-II and LC3-I is presented in Figure 10A,B for each blot. The ratios of the LC3 isoforms can be compared between the control (1% DMSO in ICM) and the treated cells. Ac-OT20 was selected as the model compound of the carrier peptides, and this peptide has no autophagy-stimulating effect. Treatment with ASA1 and its peptide conjugates did not induce autophagy, and the ratio of LC3-II and LC3-I did not differ from the control. In the case of

https://doi.org/10.1021/acsomega.3c05727
ACS Omega 2024, 9, 16927–16948

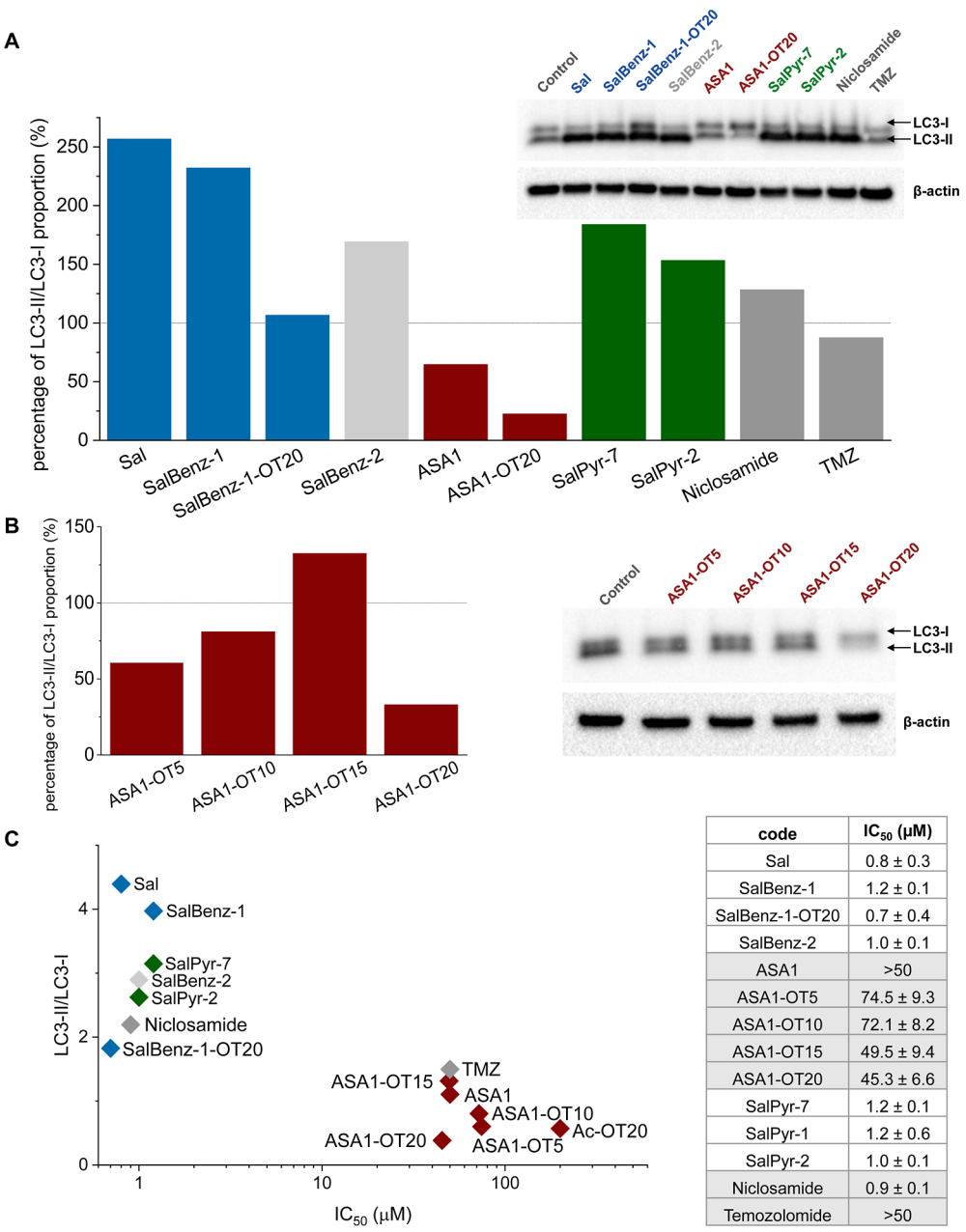

code	IC_{50} (μM)
Sal	0.8 ± 0.3
SalBenz-1	1.2 ± 0.1
SalBenz-1-OT20	0.7 ± 0.4
SalBenz-2	1.0 ± 0.1
ASA1	>50
ASA1-OT5	74.5 ± 9.3
ASA1-OT10	72.1 ± 8.2
ASA1-OT15	49.5 ± 9.4
ASA1-OT20	45.3 ± 6.6
SalPyr-7	1.2 ± 0.1
SalPyr-1	1.2 ± 0.6
SalPyr-2	1.0 ± 0.1
Niclosamide	0.9 ± 0.1
Temozolomide	>50

Figure 10. Cytostatic effect of the salicylanilide derivatives on U87 cells. Western blot and densitometry analysis of the level of autophagy-related LC3 proteins on whole-cell extracts of U87 GBM cells treated with (A) salicylanilide derivatives (10 μM) or conjugates (50 μM) and (B) ASA-tuftsin conjugates (50 μM). β-Actin was used as a loading control. (C) *In vitro* cytostatic effect of the compounds (IC_{50} values). Effect of the compounds on autophagy plotted against their cytostatic effect. Compounds with high antitumor activity have an autophagy-inducing effect.

treatment with Sal, SalBenz-1, SalBenz-1-OT20, SalBenz-2, SalPyr-7, and SalPyr-2, autophagy induction was observed. Sal and SalBenz-1 have the highest autophagy-inducing effect. Interestingly, the conjugate SalBenz-1-OT20 has limited autophagy induction. SalBenz-2, which is structurally similar to SalBenz-1, also induced autophagy, but to a lower extent. Niclosamide and TMZ were used as model compounds of clinical application, among which only niclosamide had an autophagy-inducing effect. The parent salicylanilide derivative, the salicylanilide 4-formylbenzoates, and the salicylanilide 5-chloropyrazinoates have similar or higher autophagy-inducing effects than the clinical agent niclosamide.

***In Vitro* Cytostatic Activity of Compounds.** MTT assay was applied to determine the cytostatic activity of the compounds on human U87 GBM cells. The IC_{50} values (the concentration at which the viability of the cells decreases to 50% from the maximal viability) were determined from the dose−response curves. Compounds that induce autophagy (Sal, SalBenz-1, SalBenz-1-OT20, SalBenz-2, SalPyr-7, SalPyr-2, and niclosamide) inhibit the growth of GBM cells in low concentrations (0.7−1.2 μM, Figure 10C). ASA1 and the conjugates ASA1-OT5, ASA1-OT10, ASA1-OT15, ASA1-OT20, and TMZ have no or only slight *in vitro* cytostatic effect on U87 cells. The cytostatic effect of the ASA1-OT20 conjugate can be a consequence of the enhanced cellular uptake of the salicylanilide derivative as the OT20 peptide has the highest internalization on U87 cells. The liberation of the active compound from the conjugates is also necessary for the

https://doi.org/10.1021/acsomega.3c05727
ACS Omega 2024, 9, 16927−16948

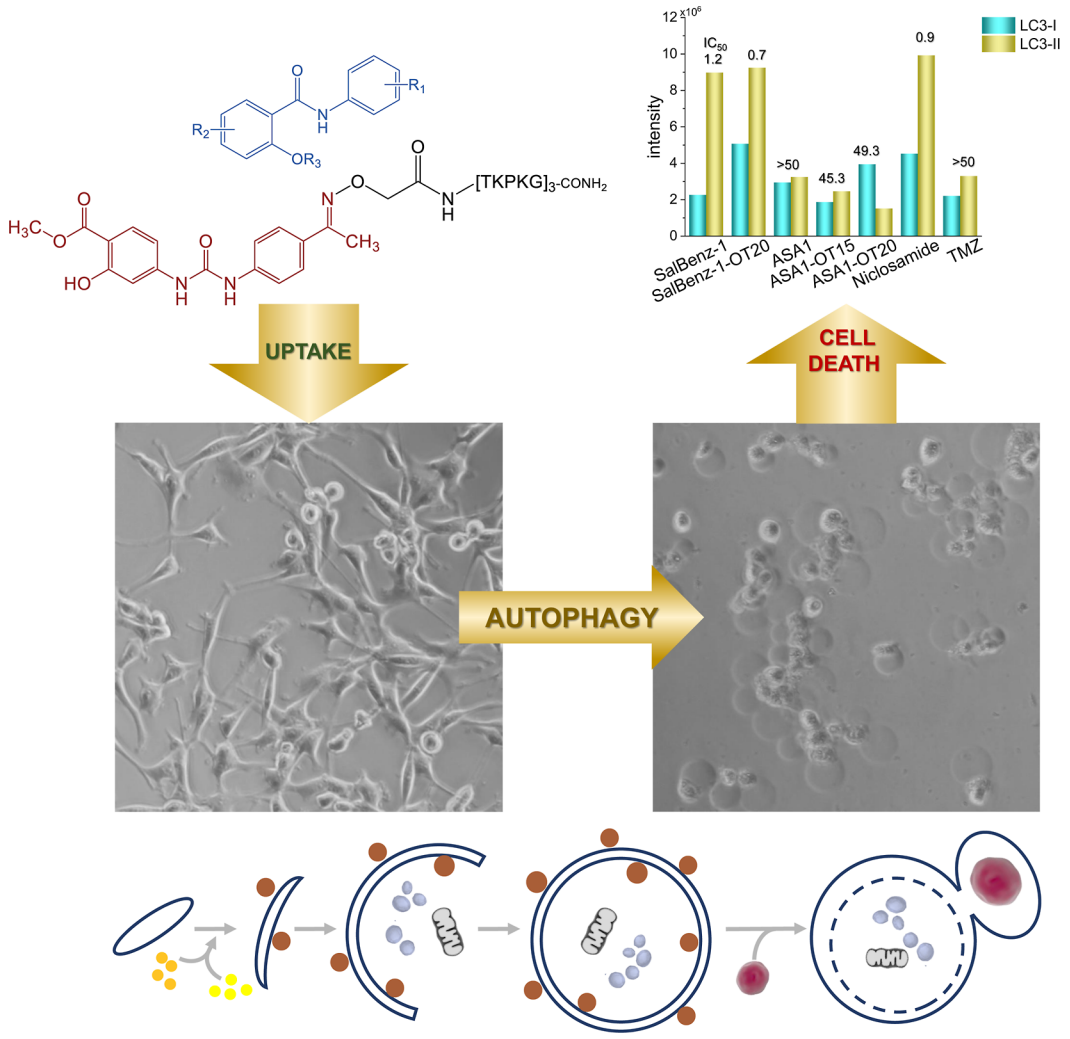

Figure 11. Novel salicylanilide derivatives with antitumor effects on U87 human GBM cells were identified in this study. The compounds with the antitumor effect induce autophagy processes. To enhance the internalization of the compounds, selected salicylanilide derivatives were conjugated to tuftsin carrier peptides. Peptide conjugates have an increased antitumor effect compared to the parent salicylanilides.

cytostatic effect. Degradation of the proposed conjugates in rat liver lysosomal homogenate can be seen in Supporting Information Figure S23. In the case of TMZ, the lack of effect can be related to its low cellular uptake (data not shown). Substituted salicylanilide (Sal), salicylanilide 5-chloropyrazinoates (SalPyr-1, SalPyr-2, and SalPyr-7), and the salicylanilide 4-formylbenzoates (SalBenz-1, SalBenz-1-OT20, and SalBenz-2) have similar *in vitro* autophagy-inducing and cytostatic profiles to that of niclosamide, a salicylanilide derivative with GBM-inhibiting effect. However, when tested on a nontumor cell model (murine bone marrow-derived macrophages), the salicylanilide derivatives showed only a slight cytotoxic effect (data not shown), holding the promise to have potential selectivity toward cancer cells.

CONCLUSIONS

GBM multiforme is a highly aggressive and deadly human tumor, characterized by a high proliferative rate and unresponsiveness to chemotherapy. Therefore, new compounds against aggressive GBM are immensely needed. Salicylanilides have multiple mechanisms of action, and they were identified as highly or moderately cytotoxic to mammalian cells.[60,62] For the present investigation, a parent salicylanilide (Sal), a 4-aminosalicylic acid derivative (ASA), salicylanilide 5-chloropyrazinoates (SalPyr), and two new salicylanilide 4-formylbenzoates (SalBenz) were chemically and *in vitro* characterized. Peptide conjugates of the 4-aminosalicylic acid derivative and one of the new salicylanilide 4-formylbenzoates were synthesized for better bioavailability. We demonstrated that conjugation of carrier peptides increased the solubility. Employing lysosomal digestion, we analyzed the degradation process which was necessary for the antitumor effect. As peptide carriers, tuftsin derivatives ($[TKPKG]_n$, $n = 1-4$) were used. These peptides are ligands for the NRPs and internalized into GBM cells. To characterize the carrier peptides, the internalization and localization of the Cf-tuftsin derivatives were determined. In all cases, time- and concentration-dependent internalization was observed, and UC_{50} values were calculated to compare the carrier peptides. Localization study by confocal laser scanning microscopy confirmed that Cf-tuftsin derivatives internalized (at least partially) through endocytosis. Most clinical and experimental antiglioma agents face hindered transport through the blood–brain barrier and poor tumor tissue penetration. To circumvent these problems, drug–targeting peptide conjugates of these compounds can be employed. Tuftsin derivatives were applied

https://doi.org/10.1021/acsomega.3c05727
ACS Omega 2024, 9, 16927−16948

to target the NRP-1 transport system for selectivity, better bioavailability, and tumor penetration. Therefore, we have also studied the Cf-tuftsins as targeting candidates on a simple blood−brain barrier TW-based HUVEC-U87 coculture model. However, only the OT20 tuftsin derivative showed slight penetration ability on the HUVEC-U87 coculture system. It is important to note that both OT15 and OT20 derivatives possessed fair internalization ability on U87 spheroids applied as simple, bulky tumor tissue mimics. To overcome the limited barrier transport ability of tuftsin carriers, we can combine their beneficial properties (selectivity and no cytotoxicity), building them into tandem sequences (tuftsin and cell-penetrating peptide segments in carrier candidates).

The antitumor effect of the salicylanilides and the peptide conjugates was determined on U87 cells. Except for ASA and ASA-conjugates, compounds significantly decreased the viability of U87 cells in remarkably low concentrations (IC_{50} < 1.5 μM). The conjugate of SalBenz-1 has slightly lower IC_{50} than the parent compound, probably due to the enhanced internalization and solubility. The compounds' and conjugates' effect on autophagy was studied using the Western blot method by detection of LC3-I and LC3-II autophagy markers. To enumerate the ratio of the LC3 isoforms, a densitometry analysis was performed. Autophagy can protect cancer cells, allowing them to survive in unfavorable conditions, such as exposure to cytostatic or cytotoxic drugs. Autophagy has been recently established as a tumor-suppressive mechanism, displaying cancer cell-inhibiting activity. Our data demonstrated that autophagy is involved in antitumor responses on salicylanilide derivatives. The compounds with antitumor effect activity induced autophagy in U87 cells (Figure 11) Further studies are required to comprehend the details of the molecular mechanisms of the antitumorigenic action of the salicylanilide derivatives and to assess their therapeutic potential in GBM treatment.

In conclusion, our study shows autophagy as a suppressive mechanism leading to cell death. More research is required to investigate the exact mechanism of the cell death.

■ ASSOCIATED CONTENT

Supporting Information

The Supporting Information is available free of charge at https://pubs.acs.org/doi/10.1021/acsomega.3c05727.

> Effect of autophagy modulators on brain cancer cell cultures, names and identifiers of salicylanilide derivatives, chemical characterization of tuftsin derivatives, fluorescence properties of the Cf-peptides, monitoring conjugation reactions through oxime bond formation, chemical characterization of conjugates, synthesis of salicylanilide derivatives, chemical characterization of salicylanilide derivatives, stability of salicylanilide derivatives in DMSO, stability of salicylanilide derivatives in RPMI-1640 incomplete medium, *in vitro* internalization of the Cf-tuftsin derivatives on U87 cells, lysosomal degradation pattern of conjugates, comparison of cellular uptake of Cf-tuftsin peptides imaged in fixed and living cells, validation of HUVEC monolayers, *in vitro* internalization of the Cf-tuftsin derivatives on HUVEC cells, *in vitro* penetration of the Cf-tuftsin derivatives through the HUVEC monolayer, *in vitro* internalization of the Cf-tuftsin derivatives on Hoechst-labeled and nonlabeled cells, and spheroid aggregation process (PDF)

■ AUTHOR INFORMATION

Corresponding Author

Szilvia Bősze − *ELKH-ELTE Research Group of Peptide Chemistry, Eötvös Loránd Research Network, Eötvös Loránd University, Budapest 1117, Hungary;* orcid.org/0000-0001-9555-699X; Phone: +36-1-3722500/1911; Email: szilvia.bosze@ttk.elte.hu

Authors

Lilla Horváth − *ELKH-ELTE Research Group of Peptide Chemistry, Eötvös Loránd Research Network, Eötvös Loránd University, Budapest 1117, Hungary;* Present Address: Becton Dickinson Hungary Kft, Környe, Hungary

Beáta Biri-Kovács − *ELKH-ELTE Research Group of Peptide Chemistry, Eötvös Loránd Research Network, Eötvös Loránd University, Budapest 1117, Hungary;* Present Address: Department of Selenoprotein Research and the National Tumor Biology Laboratory, National Institute of Oncology, 1122, Budapest, Hungary; Division of Biochemistry, Department of Medical Biochemistry, Karolinska Institutet, SE-171 77, Stockholm, Sweden; orcid.org/0000-0001-5803-9969

Zsuzsa Baranyai − *ELKH-ELTE Research Group of Peptide Chemistry, Eötvös Loránd Research Network, Eötvös Loránd University, Budapest 1117, Hungary;* Present Address: Instituto de Nanociencia y Materiales de Aragón (INMA), CSIC-Universidad de Zaragoza, Zaragoza, Spain; orcid.org/0000-0002-2174-6747

Bence Stipsicz − *ELKH-ELTE Research Group of Peptide Chemistry, Eötvös Loránd Research Network, Eötvös Loránd University, Budapest 1117, Hungary; Institute of Biology, Doctoral School of Biology, Eötvös Loránd University, Budapest 1117, Hungary*

Előd Méhes − *Institute of Physics, Department of Biological Physics, Eötvös Loránd University, Budapest 1117, Hungary*

Bálint Jezsó − *Research Centre for Natural Sciences, Institute of Enzymology, Budapest 1053, Hungary; ELTE-MTA "Momentum" Motor Enzymology Research Group, Department of Biochemistry, Eötvös Loránd University, Budapest 1117, Hungary*

Martin Krátký − *Department of Organic and Bioorganic Chemistry, Faculty of Pharmacy in Hradec Králové, Charles University, 500 03 Hradec Králové, Czech Republic*

Jarmila Vinšová − *Department of Organic and Bioorganic Chemistry, Faculty of Pharmacy in Hradec Králové, Charles University, 500 03 Hradec Králové, Czech Republic*

Complete contact information is available at: https://pubs.acs.org/10.1021/acsomega.3c05727

Author Contributions

[#]L.H. and B.B.-K. have equal contribution. Conceptualization: Szilvia Bősze; methodology: Szilvia Bősze, Zsuzsa Baranyai, Lilla Horváth, Martin Krátký, and Jarmila Vinšová; synthesis, investigation, and analysis: Martin Krátký, Zsuzsa Baranyai, Lilla Horváth, Beáta Biri-Kovács, and Szilvia Bősze; confocal microscopy image acquisition and analysis: Bálint Jezsó, Lilla Horváth, and Szilvia Bősze; TW and spheroid experiments and data analysis: Bence Stipsicz, Előd Méhes, Lilla Horváth, and

https://doi.org/10.1021/acsomega.3c05727
ACS Omega 2024, 9, 16927−16948

Szilvia Bősze; Writing—original draft preparation: Szilvia Bősze and Zsuzsa Baranyai; Writing—review and editing: Lilla Horváth, Szilvia Bősze, Beáta Biri-Kovács, Bence Stipsicz, Előd Méhes, and Martin Krátký; Funding acquisition: Szilvia Bősze, Lilla Horváth, Martin Krátký, and Jarmila Vinšová. L.H. and B.B.-K. are equal contributors.

Notes

The authors declare no competing financial interest.

Ethics approval: This article does not contain any studies with human participants or animals.

■ ACKNOWLEDGMENTS

The authors are grateful for the support of the National Research, Development and Innovation Office, Hungary (grants: VEKOP-2.3.3-15-2017-00020 and TKP2020-IKA-05). This work was supported by the EFSA-CDN (grant no. CZ.02.1.01/0.0/0.0/16_019/0000841) and cofunded by the ERDF and SVV 260 661. We are grateful for the ELTE Thematic Excellence Programme (Szint+) and the 2018-1.2.1-NKP-2018-00005 project (under the 2018-1.2.1-NKP funding scheme) provided by the Hungarian Ministry for Innovation and Technology and the National Research, Development and Innovation Office, Hungary (NKFIH). We are also grateful for the support of K142904 (PI: SB, NKFIH), and LBH is grateful for the support of the ÚNKP-22-4 New National Excellence Program of the Ministry for Culture and Innovation from the source of the National Research, Development and Innovation Fund. BS is grateful for the support of the Doctoral School of Biology, Institute of Biology, Eötvös Loránd University.

■ REFERENCES

(1) Holland, E. C. Glioblastoma multiforme: the terminator. *Proc. Natl. Acad. Sci. U.S.A.* **2000**, *97*, 6242−6244.

(2) Adamson, C.; Kanu, O. O.; Mehta, A. I.; Di, C.; Lin, N.; Mattox, A. K.; Bigner, D. D. Glioblastoma multiforme: a review of where we have been and where we are going. *Expert Opin. Invest. Drugs* **2009**, *18*, 1061−1083.

(3) Kanu, O. O.; Mehta, A.; Di, C.; Lin, N.; Bortoff, K.; Bigner, D. D.; Yan, H.; Adamson, D. C. Glioblastoma multiforme: a review of therapeutic targets. *Expert Opin. Ther. Targets* **2009**, *13*, 701−718.

(4) Alifieris, C.; Trafalis, D. T. Glioblastoma multiforme: Pathogenesis and treatment. *Pharmacol. Ther.* **2015**, *152*, 63−82.

(5) Hanif, F.; Muzaffar, K.; Perveen, K.; Malhi, S. M.; Simjee, S. U. Glioblastoma Multiforme: A Review of its Epidemiology and Pathogenesis through Clinical Presentation and Treatment. *Asian Pac J. Cancer Prev.* **2017**, *18*, 3−9.

(6) Batash, R.; Asna, N.; Schaffer, P.; Francis, N.; Schaffer, M. Glioblastoma Multiforme, Diagnosis and Treatment; Recent Literature Review. *Curr. Med. Chem.* **2017**, *24*, 3002−3009.

(7) Stupp, R.; Mason, W. P.; van den Bent, M. J.; Weller, M.; Fisher, B.; Taphoorn, M. J. B.; Belanger, K.; Brandes, A. A.; Marosi, C.; Bogdahn, U.; Curschmann, J.; Janzer, R. C.; Ludwin, S. K.; Gorlia, T.; Allgeier, A.; Lacombe, D.; Cairncross, J. G.; Eisenhauer, E.; Mirimanoff, R. O. Radiotherapy plus concomitant and adjuvant Temozolomide for glioblastoma. *N. Engl. J. Med.* **2005**, *352*, 987−996.

(8) Weller, M.; Wick, W.; Aldape, K.; Brada, M.; Berger, M.; Pfister, S. M.; Nishikawa, R.; Rosenthal, M.; Wen, P. Y.; Stupp, R.; Reifenberger, G. Glioma. *Nat. Rev. Dis. Primers* **2015**, *1*, 15017.

(9) Eyler, C. E.; Rich, J. N. Survival of the fittest: cancer stem cells in therapeutic resistance and angiogenesis. *J. Clin. Oncol.* **2008**, *26*, 2839−2845.

(10) Wicha, M. S.; Liu, S.; Dontu, G. Cancer stem cells: an old idea-a paradigm shift. *Cancer Res.* **2006**, *66*, 1883−1890.

(11) Alves, T. R.; Lima, F. R. S.; Kahn, S. A.; Lobo, D.; Dubois, L. G. F.; Soletti, R.; Borges, H.; Neto, V. M. Glioblastoma cells: a heterogeneous and fatal tumor interacting with the parenchyma. *Life Sci.* **2011**, *89*, 532−539.

(12) Shergalis, A.; Bankhead, A., 3rd; Luesakul, U.; Muangsin, N.; Neamati, N. Current Challenges and Opportunities in Treating Glioblastoma. *Pharmacol. Rev.* **2018**, *70*, 412−445.

(13) Kim, H. J.; Kim, D.-Y. Present and Future of Anti-Glioblastoma Therapies: A Deep Look into Molecular Dependencies/Features. *Molecules* **2020**, *25*, 4641.

(14) Levy, J. M. M.; Towers, C. G.; Thorburn, A. Targeting autophagy in cancer. *Nat. Rev. Cancer* **2017**, *17*, 528−542.

(15) Nazio, F.; Bordi, M.; Cianfanelli, V.; Locatelli, F.; Cecconi, F. Autophagy and cancer stem cells: molecular mechanisms and therapeutic applications. *Cell Death Differ.* **2019**, *26*, 690−702.

(16) Rahman, M. A.; Saha, S. K.; Rahman, M. S.; Uddin, M. J.; Uddin, M. S.; Pang, M.-G.; Rhim, H.; Cho, S.-G. Molecular Insights Into Therapeutic Potential of Autophagy Modulation by Natural Products for Cancer Stem Cells. *Front. Cell Dev. Biol.* **2020**, *8*, 283.

(17) Rahman, M. A.; Hannan, M. A.; Dash, R.; Rahman, M. H.; Islam, R.; Uddin, M. J.; Sohag, A. A. M.; Rahman, M. H.; Rhim, H. Phytochemicals as a Complement to Cancer Chemotherapy: Pharmacological Modulation of the Autophagy-Apoptosis Pathway. *Front. Pharmacol* **2021**, *12*, 639628.

(18) Jandrey, E. H. F.; Bezerra, M.; Inoue, L. T.; Furnari, F. B.; Camargo, A. A.; Costa, E. T. A Key Pathway to Cancer Resilience: The Role of Autophagy in Glioblastomas. *Front. Oncol.* **2021**, *11*, 652133.

(19) Buzun, K.; Gornowicz, A.; Lesyk, R.; Bielawski, K.; Bielawska, A. Autophagy Modulators in Cancer Therapy. *Int. J. Mol. Sci.* **2021**, *22*, 5804.

(20) Mizushima, N. Autophagy: process and function. *Genes Dev.* **2007**, *21*, 2861−2873.

(21) Hayat, M. A. Chapter 1 - Overview of Autophagy. In *Autophagy: Cancer, Other Pathologies, Inflammation, Immunity, Infection, and Aging*; Hayat, M. A., Ed.; Academic Press: San Diego, 2016, pp 1−71.

(22) Li, W. W.; Li, J.; Bao, J. K. Microautophagy: lesser-known self-eating. *Cell. Mol. Life Sci.* **2012**, *69*, 1125−1136.

(23) Cuervo, A. M.; Wong, E. Chaperone-mediated autophagy: roles in disease and aging. *Cell. Res.* **2014**, *24*, 92−104.

(24) Noda, N. N. Atg2 and Atg9: Intermembrane and interleaflet lipid transporters driving autophagy. *Biochim. Biophys. Acta, Mol. Cell Biol. Lipids* **2021**, *1866*, 158956.

(25) Tanida, I.; Ueno, T.; Kominami, E. LC3 and Autophagy. *Methods Mol. Biol.* **2008**, *445*, 77−88.

(26) Yoshii, S. R.; Mizushima, N. Monitoring and Measuring Autophagy. *Int. J. Mol. Sci.* **2017**, *18*, 1865.

(27) Glick, D.; Barth, S.; Macleod, K. F. Autophagy: cellular and molecular mechanisms. *J. Pathol.* **2010**, *221*, 3−12.

(28) Ma, Y. Chapter 13 - Role of Autophagy in Cancer Therapy. In *Autophagy: Cancer, Other Pathologies, Inflammation, Immunity, Infection, and Aging*; Hayat, M. A., Ed.; Academic Press: San Diego, 2016, pp 231−251.

(29) Liu, H.; He, Z.; Simon, H.-U. Chapter 14 - The Role of Autophagy in Cancer and Chemotherapy. In *Autophagy: Cancer, Other Pathologies, Inflammation, Immunity, Infection, and Aging*; Hayat, M. A., Ed.; Academic Press: San Diego, 2016, pp 253−265.

(30) Janji, B.; Viry, E.; Mgrditchian, T.; Arakelian, T.; Medves, S.; Berchem, G. Chapter 15 - Autophagy Activation in the Tumor Microenvironment: A Major Process in Shaping the Antitumor Immune Response. In *Autophagy: Cancer, Other Pathologies, Inflammation, Immunity, Infection, and Aging*; Hayat, M. A., Ed.; Academic Press: San Diego, 2016, pp 267−290.

(31) Shen, S.; Codogno, P. Chapter 7 - The Role of Autophagy in Cell Death. In *Autophagy: Cancer, Other Pathologies, Inflammation, Immunity, Infection, and Aging*; Hayat, M. A., Ed.; Academic Press: San Diego, 2016, pp 139−154.

(32) Doherty, J.; Baehrecke, E. H. Life, death and autophagy. *Nat. Cell Biol.* **2018**, *20*, 1110−1117.

https://doi.org/10.1021/acsomega.3c05727
ACS Omega 2024, 9, 16927−16948

(33) Koukourakis, M. I.; Mitrakas, A. G.; Giatromanolaki, A. Therapeutic interactions of autophagy with radiation and Temozolomide in glioblastoma: evidence and issues to resolve. *Br. J. Cancer* **2016**, *114*, 485−496.
(34) Huang, H.; Song, J.; Liu, Z.; Pan, L.; Xu, G. Autophagy activation promotes bevacizumab resistance in glioblastoma by suppressing Akt/mTOR signaling pathway. *Oncol. Lett.* **2018**, *15*, 1487−1494.
(35) Golden, E. B.; Cho, H. Y.; Jahanian, A.; Hofman, F. M.; Louie, S. G.; Schonthal, A. H.; Chen, T. C. Chloroquine enhances Temozolomide cytotoxicity in malignant gliomas by blocking autophagy. *Neurosurg. Focus.* **2014**, *37*, No. E12.
(36) Jiang, H.; Gomez-Manzano, C.; Aoki, H.; Alonso, M. M.; Kondo, S.; McCormick, F.; Xu, J.; Kondo, Y.; Bekele, B. N.; Colman, H.; Lang, F. F.; Fueyo, J. Examination of the therapeutic potential of Delta-24-RGD in brain tumor stem cells: role of autophagic cell death. *J. Natl. Cancer Inst.* **2007**, *99*, 1410−1414.
(37) Jiang, Y.; Jiao, Y.; Liu, Y.; Zhang, M.; Wang, Z.; Li, Y.; Li, T.; Zhao, X.; Wang, D. Sinomenine Hydrochloride Inhibits the Metastasis of Human Glioblastoma Cells by Suppressing the Expression of Matrix Metalloproteinase-2/-9 and Reversing the Endogenous and Exogenous Epithelial-Mesenchymal Transition. *Int. J. Mol. Sci.* **2018**, *19*, 844.
(38) Rahman, M. A.; Bishayee, K.; Habib, K.; Sadra, A.; Huh, S.-O. 18α-Glycyrrhetinic acid lethality for neuroblastoma cells via de-regulating the Beclin-1/Bcl-2 complex and inducing apoptosis. *Biochem. Pharmacol.* **2016**, *117*, 97−112.
(39) Luo, G.-X.; Cai, J.; Lin, J.-Z.; Luo, W.-S.; Luo, H.-S.; Jiang, Y.-Y.; Zhang, Y. Autophagy inhibition promotes gambogic acid-induced suppression of growth and apoptosis in glioblastoma cells. *Asian Pac. J. Cancer Prev.* **2012**, *13*, 6211−6216.
(40) Liu, Y.; Chen, Y.; Lin, L.; Li, H. Gambogic Acid as a Candidate for Cancer Therapy: A Review. *Int. J. Nanomed.* **2020**, *15*, 10385−10399.
(41) Rahman, M. A.; Hwang, H.; Nah, S.-Y.; Rhim, H. Gintonin stimulates autophagic flux in primary cortical astrocytes. *J. Ginseng Res.* **2020**, *44*, 67−78.
(42) Jovanović Stojanov, S.; Kostić, A.; Ljujić, M.; Lupšić, E.; Schenone, S.; Pešić, M.; Dinić, J. Autophagy Inhibition Enhances Anti-Glioblastoma Effects of Pyrazolo[3,4-d]pyrimidine Tyrosine Kinase Inhibitors. *Life* **2022**, *12*, 1503.
(43) Jiang, J.; Zhang, L.; Chen, H.; Lei, Y.; Zhang, T.; Wang, Y.; Jin, P.; Lan, J.; Zhou, L.; Huang, Z.; Li, B.; Liu, Y.; Gao, W.; Xie, K.; Zhou, L.; Nice, E. C.; Peng, Y.; Cao, Y.; Wei, Y.; Wang, K.; Huang, C. Regorafenib induces lethal autophagy arrest by stabilizing PSAT1 in glioblastoma. *Autophagy* **2020**, *16*, 106−122.
(44) Johannessen, T.-C.; Hasan-Olive, M. M.; Zhu, H.; Denisova, O.; Grudic, A.; Latif, M. A.; Saed, H.; Varughese, J. K.; Rosland, G. V.; Yang, N.; Sundstrom, T.; Nordal, A.; Tronstad, K. J.; Wang, J.; Lund-Johansen, M.; Simonsen, A.; Janji, B.; Westermarck, J.; Bjerkvig, R.; Prestegarden, L. Thioridazine inhibits autophagy and sensitizes glioblastoma cells to Temozolomide. *Int. J. Cancer* **2019**, *144*, 1735−1745.
(45) Palumbo, P.; Lombardi, F.; Augello, F. R.; Giusti, I.; Dolo, V.; Leocata, P.; Cifone, M. G.; Cinque, B. Biological effects of selective COX-2 inhibitor NS398 on human glioblastoma cell lines. *Cancer Cell Int.* **2020**, *20*, 167.
(46) Matteoni, S.; Matarrese, P.; Ascione, B.; Ricci-Vitiani, L.; Pallini, R.; Villani, V.; Pace, A.; Paggi, M. G.; Abbruzzese, C. Chlorpromazine induces cytotoxic autophagy in glioblastoma cells via endoplasmic reticulum stress and unfolded protein response. *J. Exp. Clin. Cancer Res.* **2021**, *40*, 347.
(47) Liu, T.; Li, A.; Xu, Y.; Xin, Y. Momelotinib sensitizes glioblastoma cells to Temozolomide by enhancement of autophagy via JAK2/STAT3 inhibition. *Oncol. Rep.* **2019**, *41*, 1883−1892.
(48) Zielke, S.; Meyer, N.; Mari, M.; Abou-El-Ardat, K.; Reggiori, F.; van Wijk, S. J. L.; Kögel, D.; Fulda, S. Loperamide, pimozide, and STF-62247 trigger autophagy-dependent cell death in glioblastoma cells. *Cell Death Dis.* **2018**, *9*, 994.
(49) Yuan, B.; Shimada, R.; Xu, K.; Han, L.; Si, N.; Zhao, H.; Bian, B.; Hayashi, H.; Okazaki, M.; Takagi, N. Multiple cytotoxic effects of gamabufotalin against human glioblastoma cell line U-87. *Chem. Biol. Interact.* **2019**, *314*, 108849.
(50) Zhu, Y.; Fang, J.; Wang, H.; Fei, M.; Tang, T.; Liu, K.; Niu, W.; Zhou, Y. Baicalin suppresses proliferation, migration, and invasion in human glioblastoma cells via Ca(2+)-dependent pathway. *Drug Des. Dev. Ther.* **2018**, *12*, 3247−3261.
(51) Park, K.-R.; Jeong, Y. H.; Lee, J. Y.; Kwon, I. K.; Yun, H.-M. Anti-tumor effects of jaceosidin on apoptosis, autophagy, and necroptosis in human glioblastoma multiforme. *Am. J. Cancer Res.* **2021**, *11*, 4919−4930.
(52) Lee, J. E.; Yoon, S. S.; Moon, E. Y. Curcumin-Induced Autophagy Augments Its Antitumor Effect against A172 Human Glioblastoma Cells. *Biomol. Ther.* **2019**, *27*, 484−491.
(53) Bai, Z.-L.; Tay, V.; Guo, S.-Z.; Ren, J.; Shu, M.-G. Silibinin Induced Human Glioblastoma Cell Apoptosis Concomitant with Autophagy through Simultaneous Inhibition of mTOR and YAP. *Biomed. Res. Int.* **2018**, *2018*, 1−10.
(54) Taylor, M. A.; Khathayer, F.; Ray, S. K. Quercetin and Sodium Butyrate Synergistically Increase Apoptosis in Rat C6 and Human T98G Glioblastoma Cells Through Inhibition of Autophagy. *Neurochem. Res.* **2019**, *44*, 1715−1725.
(55) Silva, V. A. O.; Rosa, M. N.; Miranda-Gonçalves, V.; Costa, A. M.; Tansini, A.; Evangelista, A. F.; Martinho, O.; Carloni, A. C.; Jones, C.; Lima, J. P.; Pianowski, L. F.; Reis, R. M. Euphol, a tetracyclic triterpene, from Euphorbia tirucalli induces autophagy and sensitizes Temozolomide cytotoxicity on glioblastoma cells. *Invest. New Drugs* **2019**, *37*, 223−237.
(56) Zhou, N.; Wei, Z.; Qi, Z.; Chen, L. Abscisic Acid-Induced Autophagy Selectively via MAPK/JNK Signalling Pathway in Glioblastoma. *Cell. Mol. Neurobiol.* **2021**, *41*, 813−826.
(57) Cheng, Y.; Xie, P. Ganoderic acid A holds promising cytotoxicity on human glioblastoma mediated by incurring apoptosis and autophagy and inactivating PI3K/AKT signaling pathway. *J. Biochem. Mol. Toxicol.* **2019**, *33*, No. e22392.
(58) Qu, H.; Song, X.; Song, Z.; Jiang, X.; Gao, X.; Bai, L.; Wu, J.; Na, L.; Yao, Z. Berberine reduces Temozolomide resistance by inducing autophagy via the ERK1/2 signaling pathway in glioblastoma. *Cancer Cell Int.* **2020**, *20*, 592.
(59) Dong, Q.; Wang, D.; Li, L.; Wang, J.; Li, Q.; Duan, L.; Yin, H.; Wang, X.; Liu, Y.; Yuan, G.; Pan, Y. Biochanin A Sensitizes Glioblastoma to Temozolomide by Inhibiting Autophagy. *Mol. Neurobiol.* **2022**, *59*, 1262−1272.
(60) Baranyai, Z.; Biri-Kovács, B.; Krátký, M.; Szeder, B.; Debreczeni, M. L.; Budai, J.; Kovács, B.; Horváth, L.; Pári, E.; Németh, Z.; Cervenak, L.; Zsila, F.; Méhes, E.; Kiss, É.; Vinšová, J.; Bősze, S. Cellular Internalization and Inhibition Capacity of New Anti-Glioma Peptide Conjugates: Physicochemical Characterization and Evaluation on Various Monolayer- and 3D-Spheroid-Based in Vitro Platforms. *J. Med. Chem.* **2021**, *64*, 2982−3005.
(61) Waisser, K.; Bures, O.; Holy, P.; Kunes, J.; Oswald, R.; Jiraskova, L.; Pour, M.; Klimesova, V.; Kubicova, L.; Kaustova, J. Relationship between the structure and antimycobacterial activity of substituted salicylanilides. *Arch. Pharm.* **2003**, *336*, 53−71.
(62) Baranyai, Z.; Kratky, M.; Vinsova, J.; Szabo, N.; Senoner, Z.; Horvati, K.; Stolarikova, J.; David, S.; Bosze, S. Combating highly resistant emerging pathogen Mycobacterium abscessus and Mycobacterium tuberculosis with novel salicylanilide esters and carbamates. *Eur. J. Med. Chem.* **2015**, *101*, 692−704.
(63) Lal, J.; Kaul, G.; Akhir, A.; Ansari, S. B.; Chopra, S.; Reddy, D. N. Bio-evaluation of fluoro and trifluoromethyl-substituted salicylanilides against multidrug-resistant S. aureus. *Med. Chem. Res.* **2021**, *30*, 2301−2315.
(64) Borbála Horváth, L.; Krátký, M.; Pflégr, V.; Méhes, E.; Gyulai, G.; Kohut, G.; Babiczky, Á.; Biri-Kovács, B.; Baranyai, Z.; Vinšová, J.; Bősze, S. Host cell targeting of novel antimycobacterial 4-aminosalicylic acid derivatives with tuftsin carrier peptides. *Eur. J. Pharm. Biopharm.* **2022**, *174*, 111−130.

https://doi.org/10.1021/acsomega.3c05727
ACS Omega 2024, 9, 16927−16948

(65) Kratky, M.; Vinsova, J.; Buchta, V. In vitro antibacterial and antifungal activity of salicylanilide benzoates. *Sci. World J.* **2012**, *2012*, 1−7.
(66) Kratky, M.; Vinsova, J. Antiviral activity of substituted salicylanilides-a review. *Mini Rev. Med. Chem.* **2011**, *11*, 956−967.
(67) Blake, S.; Shaabani, N.; Eubanks, L. M.; Maruyama, J.; Manning, J. T.; Beutler, N.; Paessler, S.; Ji, H.; Teijaro, J. R.; Janda, K. D. Salicylanilides Reduce SARS-CoV-2 Replication and Suppress Induction of Inflammatory Cytokines in a Rodent Model. *ACS Infect. Dis.* **2021**, *7*, 2229−2237.
(68) Agrawal, V. K.; Sharma, S. Salicylanilides in the treatment of helminth diseases. *Pharmazie* **1984**, *39*, 373−378.
(69) Li, Y.; Li, P.-K.; Roberts, M. J.; Arend, R. C.; Samant, R. S.; Buchsbaum, D. J. Multi-targeted therapy of cancer by niclosamide: A new application for an old drug. *Cancer Lett.* **2014**, *349*, 8−14.
(70) Moskaleva, E. Y.; Perevozchikova, V. G.; Zhirnik, A. S.; Severin, S. E. Molecular mechanisms of niclosamide antitumor activity. *Biomed. Khim.* **2015**, *61*, 680−693.
(71) Kadri, H.; Lambourne, O. A.; Mehellou, Y. Niclosamide, a Drug with Many (Re)purposes. *ChemMedChem* **2018**, *13*, 1088−1091.
(72) Chen, W.; Mook, R. A.; Premont, R. T.; Wang, J. Niclosamide: Beyond an antihelminthic drug. *Cell Signaling* **2018**, *41*, 89−96.
(73) Barbosa, E. J.; Löbenberg, R.; de Araujo, G. L. B.; Bou-Chacra, N. A. Niclosamide repositioning for treating cancer: Challenges and nano-based drug delivery opportunities. *Eur. J. Pharm. Biopharm.* **2019**, *141*, 58−69.
(74) Zhou, J.; Jin, B.; Jin, Y.; Liu, Y.; Pan, J. The antihelminthic drug niclosamide effectively inhibits the malignant phenotypes of uveal melanoma in vitro and in vivo. *Theranostics* **2017**, *7*, 1447−1462.
(75) Li, M.; Khambu, B.; Zhang, H.; Kang, J.-H.; Chen, X.; Chen, D.; Vollmer, L.; Liu, P.-Q.; Vogt, A.; Yin, X.-M. Suppression of lysosome function induces autophagy via a feedback down-regulation of MTOR complex 1 (MTORC1) activity. *J. Biol. Chem.* **2013**, *288*, 35769−35780.
(76) Liu, Y.; Luo, X.; Shan, H.; Fu, Y.; Gu, Q.; Zheng, X.; Dai, Q.; Xia, F.; Zheng, Z.; Liu, P.; Yin, X.-M.; Hong, L.; Li, M. Niclosamide Triggers Non-Canonical LC3 Lipidation. *Cells* **2019**, *8*, 248.
(77) Balgi, A. D.; Fonseca, B. D.; Donohue, E.; Tsang, T. C.; Lajoie, P.; Proud, C. G.; Nabi, I. R.; Roberge, M. Screen for chemical modulators of autophagy reveals novel therapeutic inhibitors of mTORC1 signaling. *PLoS One* **2009**, *4*, No. e7124.
(78) Chai, W. H.; Li, Y. R.; Lin, S. H.; Chao, Y. H.; Chen, C. H.; Chan, P. C.; Lin, C. H. Antihelminthic Niclosamide Induces Autophagy and Delayed Apoptosis in Human Non-small Lung Cancer Cells In Vitro and In Vivo. *Anticancer Res.* **2020**, *40*, 1405−1417.
(79) Park, S. J.; Shin, J. H.; Kang, H.; Hwang, J. J.; Cho, D. H. Niclosamide induces mitochondria fragmentation and promotes both apoptotic and autophagic cell death. *BMB Rep.* **2011**, *44*, 517−522.
(80) Cheng, B.; Morales, L. D.; Zhang, Y.; Mito, S.; Tsin, A. Niclosamide induces protein ubiquitination and inhibits multiple pro-survival signaling pathways in the human glioblastoma U-87 MG cell line. *PLoS One* **2017**, *12*, No. e0184324.
(81) Wang, J.; Ren, X.-R.; Piao, H.; Zhao, S.; Osada, T.; Premont, R. T.; Mook, R. A.; Morse, M. A.; Lyerly, H. K.; Chen, W. Niclosamide-induced Wnt signaling inhibition in colorectal cancer is mediated by autophagy. *Biochem. J.* **2019**, *476*, 535−546.
(82) Newton, P. T. New insights into niclosamide action: autophagy activation in colorectal cancer. *Biochem. J.* **2019**, *476*, 779−781.
(83) Kaushal, J. B.; Bhatia, R.; Kanchan, R. K.; Raut, P.; Mallapragada, S.; Ly, Q. P.; Batra, S. K.; Rachagani, S. Repurposing Niclosamide for Targeting Pancreatic Cancer by Inhibiting Hh/Gli Non-Canonical Axis of Gsk3β. *Cancers* **2021**, *13*, 3105.
(84) Wieland, A.; Trageser, D.; Gogolok, S.; Reinartz, R.; Hofer, H.; Keller, M.; Leinhaas, A.; Schelle, R.; Normann, S.; Klaas, L.; Waha, A.; Koch, P.; Fimmers, R.; Pietsch, T.; Yachnis, A. T.; Pincus, D. W.; Steindler, D. A.; Brustle, O.; Simon, M.; Glas, M.; Scheffler, B. Anticancer effects of niclosamide in human glioblastoma. *Clin. Cancer Res.* **2013**, *19*, 4124−4136.
(85) Bredel, M.; Bredel, C.; Juric, D.; Duran, G. E.; Yu, R. X.; Harsh, G. R.; Vogel, H.; Recht, L. D.; Scheck, A. C.; Sikic, B. I. Tumor Necrosis Factor-α−Induced Protein 3 As a Putative Regulator of Nuclear Factor-κB−Mediated Resistance to O^6-Alkylating Agents in Human Glioblastomas. *J. Clin. Oncol.* **2006**, *24*, 274−287.
(86) Mito, S.; Cheng, B.; Garcia, B. A.; Gonzalez, D.; Ooi, X. Y.; Ruiz, T. C.; Elisarraras, F. X.; Tsin, A.; Chew, S. A.; Arriaga, M. A. SAR study of niclosamide derivatives in the human glioblastoma U-87 MG cells. *Med. Chem. Res.* **2022**, *31*, 1313−1322.
(87) Hu, M.; Ye, W.; Li, J.; Zhong, G.; He, G.; Xu, Q.; Zhang, Y. Synthesis and evaluation of salicylanilide derivatives as potential epidermal growth factor receptor inhibitors. *Chem. Biol. Drug Des.* **2015**, *85*, 280−289.
(88) Zhu, X.-F.; Wang, J.-S.; Cai, L.-L.; Zeng, Y.-X.; Yang, D. SUCI02 inhibits the erbB-2 tyrosine kinase receptor signaling pathway and arrests the cell cycle in G1 phase in breast cancer cells. *Cancer Sci.* **2006**, *97*, 84−89.
(89) Liu, J.-Z.; Hu, Y.-L.; Feng, Y.; Guo, Y.-B.; Liu, Y.-F.; Yang, J.-L.; Mao, Q.-S.; Xue, W.-J. Rafoxanide promotes apoptosis and autophagy of gastric cancer cells by suppressing PI3K/Akt/mTOR pathway. *Exp. Cell Res.* **2019**, *385*, 111691.
(90) Wen, Y.-T.; Wu, A. T.; Bamodu, O. A.; Wei, L.; Lin, C.-M.; Yen, Y.; Chao, T.-Y.; Mukhopadhyay, D.; Hsiao, M.; Huang, H.-S. A Novel Multi-Target Small Molecule, LCC-09, Inhibits Stemness and Therapy-Resistant Phenotypes of Glioblastoma Cells by Increasing miR-34a and Deregulating the DRD4/Akt/mTOR Signaling Axis. *Cancers* **2019**, *11*, 1442.
(91) Hsieh, C.-L.; Huang, H.-S.; Chen, K.-C.; Saka, T.; Chiang, C.-Y.; Chung, L. W. K.; Sung, S.-Y. A Novel Salicylanilide Derivative Induces Autophagy Cell Death in Castration-Resistant Prostate Cancer via ER Stress-Activated PERK Signaling Pathway. *Mol. Cancer Ther.* **2020**, *19*, 101−111.
(92) Imramovský, A.; Jorda, R.; Pauk, K.; Řezníčková, E.; Dušek, J.; Hanusek, J.; Kryštof, V. Substituted 2-hydroxy-N-(arylalkyl)-benzamides induce apoptosis in cancer cell lines. *Eur. J. Med. Chem.* **2013**, *68*, 253−259.
(93) Pachnikova, G.; Uldrijan, S.; Imramovsky, A.; Krystof, V.; Slaninova, I. Substituted 2-hydroxy-N-(arylalkyl)benzamide sensitizes cancer cells to metabolic stress by disrupting actin cytoskeleton and inhibiting autophagic flux. *Toxicol. In Vitro* **2016**, *37*, 70−78.
(94) Di Grazia, A.; Laudisi, F.; Di Fusco, D.; Franzè, E.; Ortenzi, A.; Monteleone, I.; Monteleone, G.; Stolfi, C. Rafoxanide Induces Immunogenic Death of Colorectal Cancer Cells. *Cancers* **2020**, *12*, 1314.
(95) Grandclement, C.; Borg, C. Neuropilins: a new target for cancer therapy. *Cancers* **2011**, *3*, 1899−1928.
(96) Prud'homme, G. J.; Glinka, Y. Neuropilins are multifunctional coreceptors involved in tumor initiation, growth, metastasis and immunity. *Oncotarget* **2012**, *3*, 921−939.
(97) Chaudhary, B.; Khaled, Y. S.; Ammori, B. J.; Elkord, E. Neuropilin 1: function and therapeutic potential in cancer. *Cancer Immunol., Immunother.* **2014**, *63*, 81−99.
(98) Guo, H.-F.; Vander Kooi, C. W. Neuropilin Functions as an Essential Cell Surface Receptor. *J. Biol. Chem.* **2015**, *290*, 29120−29126.
(99) Kamarulzaman, E. E.; Vanderesse, R.; Gazzali, A. M.; Barberi-Heyob, M.; Boura, C.; Frochot, C.; Shawkataly, O.; Aubry, A.; Wahab, H. A. Molecular modelling, synthesis and biological evaluation of peptide inhibitors as anti-angiogenic agent targeting neuropilin-1 for anticancer application. *J. Biomol. Struct. Dyn.* **2017**, *35*, 26−45.
(100) Chen, L.; Shi, Y.; Qiu, R. Neuropilin-1 (NRP-1), a Novel Molecular Target of Glioma. *J. Nanosci. Nanotechnol.* **2016**, *16*, 6657−6666.
(101) Lee, J.; Kim, E.; Ryu, S. W.; Choi, C.; Choi, K. Combined inhibition of vascular endothelial growth factor receptor signaling with Temozolomide enhances cytotoxicity against human glioblastoma cells via downregulation of Neuropilin-1. *J. Neuro-Oncol.* **2016**, *128*, 29−34.

https://doi.org/10.1021/acsomega.3c05727
ACS Omega 2024, 9, 16927−16948

(102) Sun, S.; Lei, Y.; Li, Q.; Wu, Y.; Zhang, L.; Mu, P. P.; Ji, G. Q.; Tang, C. X.; Wang, Y. Q.; Gao, J.; Gao, J.; Li, L.; Zhuo, L.; Li, Y. Q.; Gao, D. S. Neuropilin-1 is a glial cell line-derived neurotrophic factor receptor in glioblastoma. *Oncotarget* **2017**, *8*, 74019−74035.
(103) Kwiatkowski, S. C.; Guerrero, P. A.; Hirota, S.; Chen, Z.; Morales, J. E.; Aghi, M.; McCarty, J. H. Neuropilin-1 modulates TGFβ signaling to drive glioblastoma growth and recurrence after anti-angiogenic therapy. *PLoS One* **2017**, *12*, No. e0185065.
(104) Caponegro, M. D.; Moffitt, R. A.; Tsirka, S. E. Expression of neuropilin-1 is linked to glioma associated microglia and macrophages and correlates with unfavorable prognosis in high grade gliomas. *Oncotarget* **2018**, *9*, 35655−35665.
(105) Angom, R. S.; Mondal, S. K.; Wang, F.; Madamsetty, V. S.; Wang, E.; Dutta, S. K.; Gulani, Y.; Sarabia-Estrada, R.; Sarkaria, J. N.; Quinones-Hinojosa, A.; Mukhopadhyay, D. Ablation of neuropilin-1 improves the therapeutic response in conventional drug-resistant glioblastoma multiforme. *Oncogene* **2020**, *39*, 7114−7126.
(106) Douyère, M.; Chastagner, P.; Boura, C. Neuropilin-1: A Key Protein to Consider in the Progression of Pediatric Brain Tumors. *Front. Oncol.* **2021**, *11*, 665634.
(107) Zhao, L.; Chen, H.; Lu, L.; Zhao, C.; Malichewe, C. V.; Wang, L.; Guo, X.; Zhang, X. Design and screening of a novel neuropilin-1 targeted penetrating peptide for anti-angiogenic therapy in glioma. *Life Sci.* **2021**, *270*, 119113.
(108) Bagnard, D. Neuropilin: from nervous system to vascular and tumor biology; *Advances in Experimental Medicine and Biology*; Springer US, 2002; Vol. *515*.
(109) Dumond, A.; Pages, G. Neuropilins, as Relevant Oncology Target: Their Role in the Tumoral Microenvironment. *Front. Cell Dev. Biol.* **2020**, *8*, 662.
(110) von Wronski, M. A.; Raju, N.; Pillai, R.; Bogdan, N. J.; Marinelli, E. R.; Nanjappan, P.; Ramalingam, K.; Arunachalam, T.; Eaton, S.; Linder, K. E.; Yan, F.; Pochon, S.; Tweedle, M. F.; Nunn, A. D. Tuftsin binds neuropilin-1 through a sequence similar to that encoded by exon 8 of vascular endothelial growth factor. *J. Biol. Chem.* **2006**, *281*, 5702−5710.
(111) Najjar, V. A.; Nishioka, K. "Tuftsin": a natural phagocytosis stimulating peptide. *Nature* **1970**, *228*, 672−673.
(112) Najjar, V. A. Tuftsin, A Natural Activator of Phagocyte Cells: An Overview[a]. *Ann. N.Y. Acad. Sci.* **1983**, *419*, 1−11.
(113) Fridkin, M.; Najjar, V. A. Tuftsin: Its Chemistry, Biology, and Clinical Potentia. *Crit. Rev. Biochem. Mol. Biol.* **1989**, *24*, 1−40.
(114) Siemion, I. Z.; Kluczyk, A. Tuftsin: on the 30-year anniversary of Victor Najjar's discovery. *Peptides* **1999**, *20*, 645−674.
(115) Siebert, A.; Gensicka-Kowalewska, M.; Cholewinski, G.; Dzierzbicka, K. Tuftsin - Properties and Analogs. *Curr. Med. Chem.* **2017**, *24*, 3711−3727.
(116) Mezo, G.; Kalaszi, A.; Remenyi, J.; Majer, Z.; Hilbert, A.; Lang, O.; Kohidai, L.; Barna, K.; Gaal, D.; Hudecz, F. Synthesis, conformation, and immunoreactivity of new carrier molecules based on repeated tuftsin-like sequence. *Biopolymers* **2004**, *73*, 645−656.
(117) Bősze, S.; Zsila, F.; Biri-Kovacs, B.; Szeder, B.; Majer, Z.; Hudecz, F.; Uray, K. Tailoring Uptake Efficacy of HSV-1 gD Tailoring Uptake Efficacy of Hsv-1 GD Derived Carrier Peptides. *Biomolecules* **2020**, *10*, 721.
(118) Kratky, M.; Vinsova, J. Salicylanilide ester prodrugs as potential antimicrobial agents-a review. *Curr. Pharm. Des.* **2011**, *17*, 3494−3505.
(119) Krátký, M.; Vinšová, J.; Buchta, V.; Horvati, K.; Bösze, S.; Stolaříková, J. New amino acid esters of salicylanilides active against MDR-TB and other microbes. *Eur. J. Med. Chem.* **2010**, *45*, 6106−6113.
(120) Krátký, M.; Vinšová, J.; Novotná, E.; Stolaříková, J. Salicylanilide pyrazinoates inhibit in vitro multidrug-resistant Mycobacterium tuberculosis strains, atypical mycobacteria and isocitrate lyase. *Eur. J. Pharm. Sci.* **2014**, *53*, 1−9.
(121) Baranyai, Z.; Krátký, M.; Vosátka, R.; Szabó, E.; Senoner, Z.; Dávid, S.; Stolaříková, J.; Vinšová, J.; Bősz, S. In vitro biological evaluation of new antimycobacterial salicylanilide-tuftsin conjugates. *Eur. J. Med. Chem.* **2017**, *133*, 152−173.
(122) Sato, N.; Arai, S. Studies on pyrazines. 7. The synthesis of 5-chloropyrazinecarboxylic acid. *J. Heterocycl. Chem.* **1982**, *19*, 407−408.
(123) Pontén, J.; Macintyre, E. H. Long term culture of normal and neoplastic human glia. *Acta Pathol. Microbiol. Scand.* **1968**, *74*, 465−486.
(124) Kapus, A.; Grinstein, S.; Wasan, S.; Kandasamy, R.; Orlowski, J. Functional characterization of three isoforms of the Na+/H+ exchanger stably expressed in Chinese hamster ovary cells. ATP dependence, osmotic sensitivity, and role in cell proliferation. *J. Biol. Chem.* **1994**, *269*, 23544−23552.
(125) Schagger, H. Tricine-SDS-PAGE. *Nat. Protoc.* **2006**, *1*, 16−22.
(126) Itoh, M.; Nagafuchi, A.; Moroi, S.; Tsukita, S. Involvement of ZO-1 in Cadherin-based Cell Adhesion through Its Direct Binding to α Catenin and Actin Filaments. *J. Cell Biol.* **1997**, *138*, 181−192.
(127) Méhes, E.; Mornet, D.; Jancsik, V. Subcellular localization of components of the dystrophin glycoprotein complex in cultured retinal muller glial cells. *Acta Biol. Hung.* **2003**, *54*, 241−252.
(128) Mège, R. M.; Ishiyama, N. Integration of Cadherin Adhesion and Cytoskeleton at Adherens Junctions. *Cold Spring Harbor Perspect. Biol.* **2017**, *9*, a028738.
(129) Hou, T. J.; Xia, K.; Zhang, W.; Xu, X. J. ADME evaluation in drug discovery. 4. Prediction of aqueous solubility based on atom contribution approach. *J. Chem. Inf. Comput. Sci.* **2004**, *44*, 266−275.
(130) Shoghi, E.; Fuguet, E.; Bosch, E.; Ràfols, C. Solubility-pH profiles of some acidic, basic and amphoteric drugs. *Eur. J. Pharm. Sci.* **2013**, *48*, 291−300.
(131) Horvati, K.; Fodor, K.; Palyi, B.; Henczko, J.; Balka, G.; Gyulai, G.; Kiss, E.; Biri-Kovacs, B.; Senoner, Z.; Bosze, S. Novel Assay Platform to Evaluate Intracellular Killing of Mycobacterium tuberculosis: In Vitro and In Vivo Validation. *Front. Immunol.* **2021**, *12*, 750496.
(132) Dunn, K. W.; Kamocka, M. M.; McDonald, J. H. A practical guide to evaluating colocalization in biological microscopy. *Am. J. Physiol. Cell Physiol.* **2011**, *300*, C723−C742.
(133) Bolte, S.; Cordelières, F. P. A guided tour into subcellular colocalization analysis in light microscopy. *J. Microsc.* **2006**, *224*, 213−232.
(134) Polson, H. E.; de Lartigue, J.; Rigden, D. J.; Reedijk, M.; Urbe, S.; Clague, M. J.; Tooze, S. A. Mammalian Atg18 (WIPI2) localizes to omegasome-anchored phagophores and positively regulates LC3 lipidation. *Autophagy* **2010**, *6*, 506−522.

https://doi.org/10.1021/acsomega.3c05727
ACS Omega 2024, 9, 16927−16948